

---

# **Laser-driven sources of electrons and x-rays in underdense plasma: theory and simulation**

---

by Petr Valenta

Dissertation submitted to the  
Faculty of Nuclear Sciences and Physical Engineering,  
Czech Technical University in Prague,  
in partial fulfillment of the requirements for the degree of  
Doctor of Philosophy.

Prague, 2022

**supervisor:**

doc. Ing. Ondřej Klímo, Ph.D.  
Faculty of Nuclear Sciences and Physical Engineering,  
Czech Technical University in Prague,  
Břehová 7, 115 19 Prague,  
Czech Republic

**supervisor specialist:**

prof. Sergei Vladimirovich Bulanov  
Institute of Physics,  
Czech Academy of Sciences,  
Na Slovance 1999/2, 182 21 Prague,  
Czech Republic

# Abstract

We explore novel regimes of laser-plasma interaction accessible by new generation laser systems. The scientific focus is mainly devoted to enhancement of laser-generated sources of accelerated electrons and coherent short-wavelength radiation based on plasma waves driven by intense laser pulses. First we describe mechanisms for obtaining electron beams based on laser wakefield acceleration technique. We analyze the properties of the wakefield in regimes dominated by the effects of dispersion and carrier envelope phase. Discussed range of parameters is relevant for electron acceleration at high repetition rate. Second we investigate the concept of relativistic mirrors in laser plasmas. We describe the recoil effects on reflection from relativistic mirrors which is crucial for maximizing the energy of reflected radiation. We find the threshold for incident pulse energy above which the relativistic mirrors undergo significant back reaction. We also analyze the generation of coherent hard electromagnetic radiation by the reflection from the electron density singularities.

**Keywords:** laser-plasma interaction, laser wakefield acceleration, relativistic mirrors, short-wavelength radiation



# Acknowledgements



# Contents

<b>Abstract</b>	<b>3</b>
<b>Acknowledgements</b>	<b>5</b>
<b>1 Introduction</b>	<b>9</b>
1.1 Aims and motivation / objectives of the thesis / problem statement . . . . .	9
1.2 Originality and contributions / role of author . . . . .	9
1.3 List of author's publications . . . . .	9
1.3.1 Publications in peer-reviewed journals . . . . .	9
1.3.2 Publications in conference proceedings . . . . .	9
1.3.3 Book chapters . . . . .	9
1.4 Related work / previous results / state-of-the-art . . . . .	9
1.5 Outline of the thesis / structure . . . . .	9
<b>2 Physics of laser-underdense plasma interaction</b>	<b>11</b>
2.1 Equations of EM field . . . . .	11
2.2 EM waves in vacuum . . . . .	11
2.3 Gaussian beam optics . . . . .	11
2.4 Interaction with single electrons, ponderomotive force . . . . .	11
2.5 Langmuir waves, wave breaking, catastrophe theory . . . . .	11
2.6 Self-focusing, self-guiding, self-phase modulation, self-amplitude modulation .	11
<b>3 Laser-wakefield acceleration of electrons</b>	<b>13</b>
3.1 Electron interaction with Langmuir wave . . . . .	13
3.2 Electron injection mechanisms . . . . .	13
3.2.1 Injection by breaking plasma wave . . . . .	13
3.2.2 Optical injection . . . . .	13
3.2.3 Ionization injection . . . . .	13
3.3 Regimes of LWFA . . . . .	13
3.3.1 Self-modulated regime . . . . .	13
3.3.2 Blow-out regime . . . . .	13
3.4 Limitations of LWFA . . . . .	13
3.4.1 Electron dephasing length . . . . .	13
3.4.2 Pump depletion length . . . . .	13
3.4.3 Beam loading . . . . .	13
3.5 Applications of accelerated electrons . . . . .	13
<b>4 Relativistic mirrors</b>	<b>15</b>

4.1	Lorentz transform, Doppler effect . . . . .	15
4.1.1	Uniformly moving mirror . . . . .	15
4.1.2	Accelerated mirror . . . . .	15
4.1.3	Oscillating mirror . . . . .	15
4.2	Physical realization of relativistic mirrors in underdense plasma . . . . .	15
4.2.1	Langmuir wave . . . . .	15
4.2.2	Bow wave . . . . .	15
<b>5</b>	<b>Computational modeling of laser-plasma interaction</b>	<b>17</b>
5.1	Particle-in-cell method . . . . .	17
<b>6</b>	<b>Author's original results</b>	<b>19</b>
6.1	On the electromagnetic-electron rings . . . . .	19
6.2	On the laser-wakefield polarity reversal . . . . .	20
6.3	On the recoil effects of relativistic mirrors . . . . .	22
6.4	On the relativistic flying forcibly oscillating mirror . . . . .	22
<b>7</b>	<b>Conclusions and perspectives</b>	<b>23</b>
<b>A</b>	<b>Selected publications</b>	<b>25</b>
A.1	On the electromagnetic-electron rings originating from the interaction of high-power short-pulse laser and underdense plasma . . . . .	25
A.2	Polarity reversal of wakefields driven by ultrashort pulse laser . . . . .	33
A.3	Recoil effects on reflection from relativistic mirrors in laser plasmas . . . . .	40
A.4	Relativistic flying forcibly oscillating reflective diffraction grating . . . . .	50

# **Chapter 1**

## **Introduction**

- 1.1 Aims and motivation / objectives of the thesis / problem statement**
- 1.2 Originality and contributions / role of author**
- 1.3 List of author's publications**
  - 1.3.1 Publications in peer-reviewed journals**
  - 1.3.2 Publications in conference proceedings**
  - 1.3.3 Book chapters**
- 1.4 Related work / previous results / state-of-the-art**
- 1.5 Outline of the thesis / structure**



## Chapter 2

# Physics of laser-underdense plasma interaction

**2.1 Equations of EM field**

**2.2 EM waves in vacuum**

**2.3 Gaussian beam optics**

**2.4 Interaction with single electrons, ponderomotive force**

The relativistic motion of an electron in the presence of transverse electromagnetic wave

**2.5 Langmuir waves, wave breaking, catastrophe theory**

**2.6 Self-focusing, self-guiding, self-phase modulation, self-amplitude modulation**



## **Chapter 3**

# **Laser-wakefield acceleration of electrons**

### **3.1 Electron interaction with Langmuir wave**

### **3.2 Electron injection mechanisms**

#### **3.2.1 Injection by breaking plasma wave**

Homogeneous plasma

Inhomogeneous plasma

#### **3.2.2 Optical injection**

#### **3.2.3 Ionization injection**

### **3.3 Regimes of LWFA**

#### **3.3.1 Self-modulated regime**

#### **3.3.2 Blow-out regime**

### **3.4 Limitations of LWFA**

#### **3.4.1 Electron dephasing length**

#### **3.4.2 Pump depletion length**

#### **3.4.3 Beam loading**

### **3.5 Applications of accelerated electrons**



# Chapter 4

## Relativistic mirrors

### 4.1 Lorentz transform, Doppler effect

#### 4.1.1 Uniformly moving mirror

#### 4.1.2 Accelerated mirror

#### 4.1.3 Oscillating mirror

### 4.2 Physical realization of relativistic mirrors in under-dense plasma

#### 4.2.1 Langmuir wave

#### 4.2.2 Bow wave



## Chapter 5

# Computational modeling of laser-plasma interaction

### 5.1 Particle-in-cell method



# Chapter 6

## Author's original results

In this chapter, the reader can find an overview of the main results achieved within the author's postgraduate studies. In total, we select four papers published in peer-reviewed journals which are fully (or from the most part) based on the author's original work. Below, we provide a brief summary of each selected paper as well as a detailed description of the author's role and contributions. The full text of all the selected publications is enclosed in Appendix A.

### 6.1 On the electromagnetic-electron rings

First, we present the results of research devoted to the coupled electromagnetic and electron rings originating from the interaction of high-power short-pulse laser and underdense plasma, which has been published in Ref. [1] (the reader can find the full text of the paper in Appendix A.1). This research has been initiated after the experimental observation of stable and tunable ring-shaped beams of high-energy electrons; the experiment has been carried out by the ELI electron acceleration group at the Institute of Plasma Physics and Laser Microfusion in Warsaw, Poland (the reader can find further details in Ref. [1]). Our preliminary goal was to find out and describe the underlying physical mechanisms which lead to the formation of ring-shaped electron beams in laser plasmas. Although several mechanisms that may result in the electron rings of similar parameters were already identified and presented in literature at that time (see, e.g., Refs. [2]), none of them seemed to correspond to the particular experimental parameters used in [1].

In general, this work investigates the propagation of high-power short-pulse laser in a low-density plasma, which is a topic relevant to a number of scientific challenges, such as laser-driven acceleration of charged particles [3], development of sources of hard electromagnetic radiation [4], and nuclear fusion within the framework of the fast ignition concept [5]. For many of these applications, it is essential that the laser pulse propagates over extended distances and transmits its energy into the plasma in controlled way without incurring excessive losses. In this context, much of the attention has been focused on the evolution of the radial profile of the laser beam in a fully ionized plasma; it turned out that the process of self-focusing for high-power laser pulses may lead to the formation of the multifilament and, in particular, ring-shaped transverse structures [6]. We show that these electromagnetic rings can become a source of high-energy ring-shaped electron beams.

In addition to the applications mentioned above, the understanding of the physical processes that lead to the generation of the electromagnetic and electron ring structures is

important due to the following reasons: (i) the electromagnetic rings may carry off a significant fraction of energy from the driver, and thus limit the overall efficiency of applications based on the laser-plasma interaction; (ii) the electron beams accelerated in the wake of the electromagnetic rings may cause a damage to surrounding equipment (e.g., capillaries used for the laser pulse guiding) and become a source of unwanted electromagnetic radiation; and (iii) the knowledge of the origin of the electromagnetic and electron rings could serve as a diagnostics for determining the regimes of laser-plasma interaction.

The first part of the paper presents an analytical model based on geometric optics approximation which qualitatively illustrates the origin and the initial stage of the electromagnetic ring formation. We define the plasma density distribution within the Langmuir wave as well as the Hamiltonian for the photon interaction with the Langmuir wave; the trajectories of photons are then obtained by solving the Hamilton equations. The second part of the paper presents a three-dimensional particle-in-cell simulation, the results of which demonstrate the formation of the electromagnetic as well as electron ring. We discuss the mechanism of formation of the electromagnetic ring and the processes of electron injection into the accelerating phase of the secondary wakefield generated by the electromagnetic ring. Finally, the third part of the paper contains the results of a systematic multi-parametric simulation study for various plasma densities, laser intensities, and laser spot sizes revealing the relationships among the properties of the electromagnetic rings and the parameters of laser and plasma.

The main results of the paper can be summarized as follows. We identify and describe a novel physical mechanism which leads to the formation of ring-shaped electromagnetic-electron structures, where the electromagnetic rings arise from the laser pulse defocusing induced by the excitation of Langmuir waves in underdense plasma, and the ring-shaped electron beams are formed and accelerated subsequently by the secondary toroidal wakefields generated by the electromagnetic rings. We further reveal that the electromagnetic rings are relatively robust nonlinear objects, whose properties can be controlled by tuning the parameters of laser and plasma. Within the studied parameter range, we find that up to  $\approx 70\%$  of the total initial driver pulse energy can be carried off by the electromagnetic rings having the opening angles  $\approx 50 - 105$  mrad.

Besides Ref. [POP], a portion of this work has been also published in Ref. [SPIE] and presented by the author at "SPIE Optics+Optoelectronics 2021", "OPTO2021 Symposium on Photon and Beam Science", and "ELI Summer school 2021", whereas the latter presentation has been awarded by the "Best poster prize". The author contributed to all the aspects of the research, including the initial formulation of the scientific topic, development of the analytical model, setup and execution of the numerical simulations on computer clusters, and analysis and interpretation of the simulation data. Furthermore, based on the results obtained the author prepared figures and wrote the bulk of the manuscript text, submitted the manuscript to the journal whereas serving as a corresponding author, and communicating with editors and referees until the final publication in the journal.

## 6.2 On the laser-wakefield polarity reversal

Second, we present the results of research devoted to the laser-wakefield acceleration of electrons in the regime of ultrashort pulses and near-critical density plasmas, which has been published in Ref. [] (The reader can find the full text of the paper in Appendix A.2). This research is closely related to the laser-wakefield acceleration of electrons driven by high-repetition-rate ( $\gtrsim$  kHz) laser systems (such as the L1 laser system at ELI Beamlines).

The research on laser-wakefield acceleration of electrons has been predominantly oriented on the Joule-class laser systems, which have already demonstrated their capability to produce electron beams at the multi-GeV energy scale with a relative energy spread of a few percent [], a few fs duration [], and hundreds of pC of charge [] (although not simultaneously). Recently, however, there has been a growing interest in the laser-wakefield acceleration of electrons driven by high-repetition-rate ( $\gtrsim$  kHz) laser systems since they can significantly improve certain characteristics (e.g., stability, signal-to-noise ratio, and average electron current []) required by a number of practical applications (e.g., ultrafast electron diffraction [], fs x-ray generation [], and pulsed radiolysis []). On the other hand, present-day high-repetition-rate lasers deliver (due to the constraints in technology) pulses with energy of only a few mJ. This (together with the requirements of the blow-out regime of the laser-wakefield acceleration) implies that, in order to produce high-quality relativistic electron sources, one has to use tightly-focused near-single-cycle pulses and thin near-critical density gas targets []. Such considerations constitute a great challenge not only from a technical point of view, but also in the sense of the understanding of underlying physical processes (e.g., related to the  $\lambda^3$  regime []).

In the first part of the paper we extend the standard model of the wakefield generation by considering the carrier-envelope phase shift of the driving pulse. The model shows that wakefield contains long-wavelength modulation of its amplitude. In the second part of the paper we analytically investigate the acceleration of electron by the modulated wakefield. We show that the electron energy gain depends on the initial phase of the driver and find the case for which the net energy acquired by the electron over given distance is maximal. Finally, the third part of the paper contains the setup and the results of the three-dimensional particle-in-cell simulation on the self-consistent evolution of the ultrashort laser pulse and near-critical density plasma. The simulation results are in qualitative agreement with the analytical model.

The main results of the paper can be summarized as follows. We reveal for the first time (to the best of our knowledge) that the wakefield, being excited by an ultrashort laser pulse in plasma, periodically reverses its polarity. As shown by the analytical model and numerical simulation, the wakefield polarity reversal is caused by dispersion and the corresponding difference between the propagation speed of the carrier and the envelope of the driving pulse. Further, we show that the novel phenomenon of the wakefield polarity reversal occurs on spatial scales shorter than the dephasing length and, therefore, significantly affects the energy spectra of accelerated electron beams. In the nonlinear regime, however, there may exist a case for which the polarity reversal length is equal to the dephasing length. In such a case, the dephasing limit is overcome and the electrons are accelerated until the energy of the driver pulse depletes. The discovery of this phenomenon is crucial for better control of the parameters of electron beams accelerated via the laser-wakefield mechanism (e.g., by adjusting the initial phase of the driver or by controlling the phase of the electron injection), particularly in experiments carried out with present-day high-repetition-rate laser systems.

Besides Ref. [PRE], a portion of this work has been also published in Refs. [Lazzarini + book, SPIE, EPS] and presented by the author at "ELI Users' conference 2020", "SPIE Optics+Optoelectronics 2019", and "EPS Conference on Plasma Physics 2018", whereas the latter presentation has been awarded by the "Best poster prize". The author contributed to all the aspects of the research, including the initial formulation of the scientific topic, development of the analytical model, setup and execution of the numerical simulations on computer clusters, and analysis and interpretation of the simulation data. Furthermore, based on the results obtained the author prepared figures and wrote the bulk of the manuscript text, submitted the manuscript to the journal whereas serving as a corresponding author, and

communicating with editors and referees until the final publication in the journal.

### **6.3 On the recoil effects of relativistic mirrors**

Third,

### **6.4 On the relativistic flying forcibly oscillating mirror**

The last publication introduces a novel scheme of the relativistic flying mirrors

## **Chapter 7**

# **Conclusions and perspectives**



## Appendix A

### Selected publications

A.1 On the electromagnetic-electron rings originating from the interaction of high-power short-pulse laser and underdense plasma



## Polarity reversal of wakefields driven by ultrashort pulse laser

P. Valenta<sup>1,2,\*</sup>, T. Zh. Esirkepov<sup>1,3</sup>, J. K. Koga<sup>1,3</sup>, A. Nečas<sup>4</sup>, G. M. Grittani<sup>1</sup>, C. M. Lazzarini<sup>1</sup>, O. Klimo<sup>1,2</sup>, G. Korn<sup>1</sup>, and S. V. Bulanov<sup>1,3</sup>

<sup>1</sup>ELI Beamlines, Institute of Physics of the Czech Academy of Sciences, Na Slovance 2, Prague 18221, Czech Republic

<sup>2</sup>Faculty of Nuclear Sciences and Physical Engineering, Czech Technical University in Prague, Brehova 7, Prague 11519, Czech Republic

<sup>3</sup>Kansai Photon Science Institute, National Institutes for Quantum and Radiological Science and Technology, Umemidai 8-1-7, Kizugawa, Kyoto 619-0215, Japan

<sup>4</sup>TAE Technologies, Pauling 19631, Foothill Ranch, California 92610, USA



(Received 7 July 2020; revised 3 September 2020; accepted 25 October 2020; published 30 November 2020)

Using an analytical model and computer simulation, we show that the wakefield driven by an ultrashort laser pulse in high-density plasma periodically reverses its polarity due to the carrier-envelope phase shift of the driver. The wakefield polarity reversal occurs on spatial scales shorter than the typical length considered for electron acceleration with the laser-wakefield mechanism. Consequently, the energies of accelerated electrons are significantly affected. The results obtained are important for the laser-wakefield acceleration under the conditions relevant to present-day high-repetition-rate laser systems.

DOI: [10.1103/PhysRevE.102.053216](https://doi.org/10.1103/PhysRevE.102.053216)

### I. INTRODUCTION

Laser-wakefield acceleration (LWFA) is a well-established technique for producing high-energy electrons in plasma [1,2]. Over the past few decades, the quality of electron beams accelerated via LWFA has rapidly evolved mainly due to the advances in technology and better understanding of the underlying physics. As of 2020, LWFA has demonstrated (although not simultaneously) the capability to produce electron beams at the multi-GeV energy scale with a relative energy spread of a few percent [3,4], a few fs duration [5–8], and hundreds of pC of charge [9,10]. These achievements make LWFA increasingly attractive for a wide range of multidisciplinary experiments and applications (e.g., radiography [11], radiotherapy [12], and radiolysis [12,13]).

Recently, there has been a growing interest in LWFA driven by high-repetition-rate ( $\gtrsim$ kHz) laser systems since they can significantly improve certain characteristics (e.g., stability, signal-to-noise ratio, and average electron current [14]) required by a number of practical applications (e.g., ultrafast electron diffraction [15,16], fs x-ray generation [17,18], and pulsed radiolysis [19]). In order to produce high-quality relativistic LWFA electron sources with present-day kHz lasers, one should use tightly focused, near-single-cycle pulses and thin, near-critical density gas targets [14,20]. Such considerations constitute a great challenge not only from a technical point of view, but also in the sense of the understanding of underlying physical processes (e.g., related to the  $\lambda^3$  regime [21]).

The LWFA of electrons at kHz using laser pulses with energies  $<10$  mJ has been pursued by several groups [22–24]. The specificities of the corresponding laser-plasma

interaction, particularly the effects of the driver carrier-envelope phase (CEP) on the electron beam dynamics [25], the electron injection [26], and the electron energy spectra [14,27], were investigated. In this paper, we present the results of analytical and numerical study of the wakefield driven by an ultrashort laser pulse in high-density plasma. We show that the wakefield polarity periodically reverses due to the CEP shift of the driving pulse which significantly affects the energies of electrons accelerated via LWFA under the conditions relevant to current high-repetition-rate lasers.

### II. DISPERSION AND CARRIER-ENVELOPE PHASE SHIFT EFFECTS

The propagation of a small amplitude electromagnetic wave in collisionless plasma is governed by the dispersion equation  $\omega^2 = 1 + k^2$ . The frequency,  $\omega$ , and wave number,  $k$ , of the electromagnetic wave are measured in the units of  $\omega_p$  and  $\omega_p/c$ , respectively, where  $\omega_p = \sqrt{4\pi n_0 e^2/m_e}$  is the Langmuir frequency,  $c$  is the speed of light in vacuum,  $n_0$  is the ambient electron number density,  $e$  is the elementary charge, and  $m_e$  is the electron mass. The phase and group velocities of the electromagnetic wave (in the units of  $c$ ) are equal to  $\beta_{ph} = \sqrt{1 + k^2}/k$  and  $\beta_g = k/\sqrt{1 + k^2}$ , respectively. As one may see,  $\beta_{ph}\beta_g = 1$ .

In dispersive media, the phase and group velocities are not equal to each other,  $\beta_{ph} \neq \beta_g$ , which causes the evolution of the driver CEP. The characteristic time scale of the CEP shift effects can be expressed by a typical dispersion time,  $t_{disp}$ , defined as the time span needed to acquire the CEP shift of the driver equal to  $\pi$ ,

$$t_{disp} = \pi/\omega(\beta_{ph} - \beta_g) = \pi\beta_g/\omega(1 - \beta_g^2). \quad (1)$$

The driver field during the time interval  $<t_{disp}$  can be in one-dimensional (1D) geometry approximated by the vector

\*petr.valenta@eli-beams.eu

potential of the following form:

$$a = a_0 \frac{\sin [\Delta k(x - \beta_g t)]}{\Delta k(x - \beta_g t)} \cos [k_c(x - \beta_{\text{ph}} t) + \varphi]. \quad (2)$$

Here,  $a_0$  is the peak vacuum amplitude of the driver normalized by  $m_e c^2/e$  and  $\varphi$  is the phase of the carrier wave. The driver wave numbers are assumed to lie within a finite band  $k_c - \Delta k < k < k_c + \Delta k$ , with  $\Delta k \ll k_c$ . The spatial coordinate,  $x$ , and time,  $t$ , are measured in units of  $c/\omega_p$  and  $\omega_p^{-1}$ , respectively.

While propagating in plasma, the driver excites a wakefield that can be described by the following system of equations [2]:

$$\partial_t p + v \partial_x p = -E + F, \quad (3)$$

$$\partial_t E + v \partial_x E = v. \quad (4)$$

Here  $p$  is the  $x$  component of the electron momentum normalized by  $m_e c$ ,  $E$  is the  $x$  component of the electric field normalized by  $E_p = m_e \omega_p c/e$ , and  $v = p/\gamma$  with  $\gamma$  being the electron Lorentz factor. This yields

$$F = -(1/2\gamma) \partial_x a^2 \quad (5)$$

for the driving force (in the units of  $m_e \omega_p c$ ) with  $a(x, t)$  given by Eq. (2). The transverse component of the generalized momentum is conserved (i.e.,  $p_\perp - a = \text{const}$ ) and, therefore,  $\gamma = \sqrt{1 + a^2 + p^2}$ . In the following, we assume that  $\gamma = 1$  (i.e., the laser-plasma interaction regime is well below the wake wave breaking threshold). The nonlinear case is addressed by numerical simulation in the second part of the paper.

The system of Eqs. (3) and (4) can be solved, e.g., using Lagrange coordinates,  $x_0$  and  $\tau$ . The relation between the Euler and Langrange coordinates is defined as  $t = \tau$  and  $x = x_0 + \xi(x_0, \tau)$ , where  $x_0$  is the initial coordinate of the fluid element (at  $t = 0$ ) and  $\xi$  is a displacement of the fluid element from its initial position,  $x_0$ , to the point  $x$  during the time  $t$ ; thus  $\partial_\tau \xi = v$ . Assuming that  $\xi \ll x_0$ , the solution in quadratures reads

$$p + iE = \int_0^\tau \frac{a_0^2 k_c}{2} e^{i(\tau-\tau')} \left( \frac{\sin [\Delta k(x_0 - \beta_g \tau')]}{\Delta k(x_0 - \beta_g \tau')} \right)^2 \times \sin [2k_c(x_0 - \beta_g^{-1} \tau') + 2\varphi] d\tau'. \quad (6)$$

In the ultrashort driver pulse limit, the solution (being transformed back to the Euler coordinates) becomes

$$p = -\frac{a_0^2}{2\beta_g} \frac{k_c}{\Delta k} \cos \left( \frac{x - \beta_g t}{\beta_g} \right) \sin \left( 2k_c \frac{1 - \beta_g^2}{\beta_g^2} x - 2\varphi \right), \quad (7)$$

$$E = \frac{a_0^2}{2\beta_g} \frac{k_c}{\Delta k} \sin \left( \frac{x - \beta_g t}{\beta_g} \right) \sin \left( 2k_c \frac{1 - \beta_g^2}{\beta_g^2} x - 2\varphi \right), \quad (8)$$

where  $0 < x \leq \beta_g t$  and  $t \geq 0$ .

As can be seen from Eqs. (7) and (8), the ultrashort driver pulse in plasma excites the wakefield of a wavelength  $\lambda_w = 2\pi\beta_g$  propagating with the phase velocity,  $\beta_w$ , equal to the group velocity of the driver,  $\beta_w = \beta_g$ . In addition to the standard model, the wakefield contains a sinusoidal modulation of the amplitude due to the slippage of the driver CEP. The

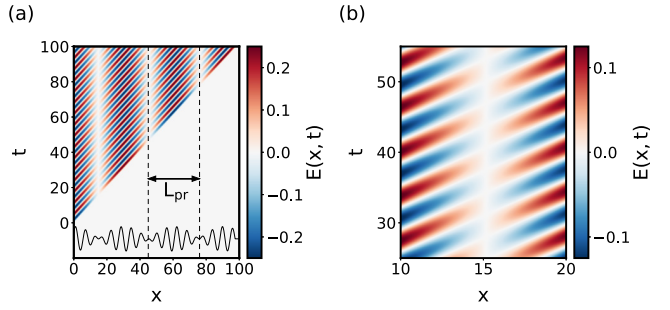


FIG. 1. Wakefield,  $E(x, t)$ , distribution in the  $(x, t)$  plane according to Eq. (8). The parameters of the driver are  $\beta_g = 0.975$ ,  $a_0 = 0.5$ ,  $k_c = 1$ ,  $\Delta k = 0.5$ , and  $\varphi = 3\pi/4$  and the plasma is homogeneous with  $n_0 = 0.5n_c$ . Panel (a) shows the periodic reversal of the wakefield polarity with  $L_{\text{pr}} \simeq 30.24$  (marked by dashed lines); the detail of the wakefield polarity reversal is shown in (b). The solid line at the bottom of (a) shows the line-out of the wakefield along the axis  $t = 100$ .

modulation wavelength, given by  $\lambda_{\text{mod}} = \pi \beta_g^2/k_c(1 - \beta_g^2)$ , corresponds to the propagation length of the driver required to shift its CEP by the factor of  $\pi$  [compare with Eq. (1)]. As a consequence, the wakefield polarity periodically reverses. The range between two adjacent longitudinal coordinates at which the wakefield polarity reversal occurs is expressed by the polarity reversal length,

$$L_{\text{pr}} = \lambda_{\text{mod}}/2 = \pi \beta_g^2/2k_c(1 - \beta_g^2). \quad (9)$$

Figure 1 shows the wakefield distribution in the  $(x, t)$  plane according to Eq. (8). The parameters of the driver are  $\beta_g = 0.975$ ,  $a_0 = 0.5$ ,  $k_c = 1$ ,  $\Delta k = 0.5$ , and  $\varphi = 3\pi/4$  and the plasma is homogeneous with  $n_0 = 0.5n_c$ , where  $n_c = n_0 \omega^2$  stands for the critical plasma density. In panel (a), one may see the periodic reversal of the wakefield polarity with  $L_{\text{pr}} \simeq 30.24$ . Panel (b) shows the detail of the wakefield polarity reversal.

### III. ELECTRON ACCELERATION BY MODULATED WAKEFIELD

As is well known, the energy of the LWFA accelerated electron is limited by the value determined by the dephasing length,

$$L_d = \pi \beta_g/(1 - \beta_g). \quad (10)$$

Following from the model, the polarity reversal length is (in underdense plasma) always shorter than the dephasing length,  $L_{\text{pr}} < L_d$ . A comparison between  $L_{\text{pr}}$  and  $L_d$  defined by Eqs. (9) and (10), respectively, is shown in Fig. 2.

The wakefield polarity reversal in its turn affects the energy of the accelerated electron. For illustration, let us consider a relativistic electron traversing the wakefield with velocity approaching the speed of light. The net change of the kinetic energy of the electron moving along the path from  $x_0 = 0$  to

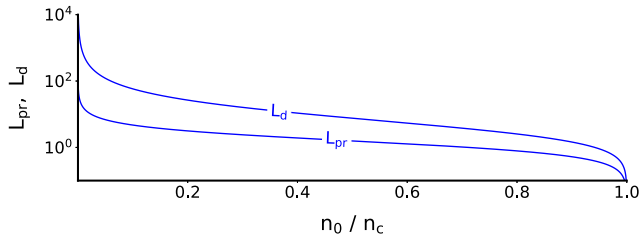


FIG. 2. Comparison between the polarity reversal length,  $L_{\text{pr}}$ , and the dephasing length,  $L_d$ , defined by Eqs. (9) and (10), respectively, in the whole range of underdense plasma.

$x_1 = x$  (in the units of  $m_e c^2$ ) is given by

$$\begin{aligned} \Delta\mathcal{E}(x) &= \int_0^x E(x', t = x') dx' \\ &= \frac{a_0^2}{4\beta_g} \frac{k_c}{\Delta k} \frac{\cos(\alpha^- x + 2\varphi) \sin(\alpha^- x)}{\alpha^-} \\ &\quad - \frac{a_0^2}{4\beta_g} \frac{k_c}{\Delta k} \frac{\cos(\alpha^+ x - 2\varphi) \sin(\alpha^+ x)}{\alpha^+}, \end{aligned} \quad (11)$$

with the coefficients  $\alpha^+$  and  $\alpha^-$  equal to

$$\alpha^\pm = \frac{\pi}{2} \left( \frac{1}{L_d} \pm \frac{1}{L_{\text{pr}}} \right). \quad (12)$$

The energy change of the electron described by Eq. (11) is shown in Fig. 3. The electron is traversing the wakefield given by Eq. (8) for the same parameters of the driver and plasma as in Fig. 1 (solid line). As can be seen, the electron either gains or loses energy over the distance of  $L_{\text{pr}} \simeq 30.24$  due to the periodic reversal of the wakefield polarity. The energy balance of the electron over  $L_d \simeq 122.52$  is  $\Delta\mathcal{E} \simeq -1.29$ . Using the standard model (i.e., neglecting the wakefield polarity reversal), the electron would theoretically gain the energy of  $\Delta\mathcal{E} \simeq 20$  over the same distance. Since  $L_{\text{pr}} \ll L_d$ , the electron energy gain under the considered conditions is always lower than the maximum value determined by the standard model.

It follows from Eq. (11) that the energy gain depends on the initial phase of the driver,  $\varphi$ . Therefore, one may find (by examining the function extrema) an optimal phase of the driver,  $\varphi_{\text{opt}}$ , for which the net energy acquired by the electron over given distance is maximal. Provided that the electron injection is localized at  $x = 0$  and the acceleration takes place

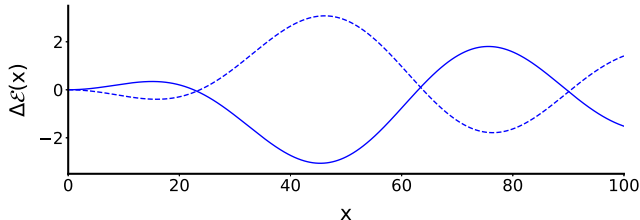


FIG. 3. Energy change of the relativistic electron,  $\Delta\mathcal{E}(x)$ , according to Eq. (11). The solid line shows the energy change of electron traversing the wakefield described by Eq. (8) for the same parameters of the driver and plasma as in Fig. 1. The dashed line shows the energy change of electron for  $\varphi = \varphi_{\text{opt}}$ .

over  $L_d$ ,

$$\varphi_{\text{opt}}^n = \frac{\pi}{4} \left( 1 + \frac{L_d}{L_{\text{pr}}} \right) + n\pi, \quad n \in \mathbb{Z}. \quad (13)$$

The energy change of the electron for  $\varphi = \varphi_{\text{opt}}$  is shown in Fig. 3 by the dashed line.

#### IV. PARTICLE-IN-CELL SIMULATION

##### A. Simulation setup

Now we explore the self-consistent evolution of the ultra-short laser pulse and near-critical density plasma numerically by means of particle-in-cell (PIC) simulation in a three-dimensional (3D) Cartesian geometry. The simulation is carried out using the PIC code EPOCH [28]. The driver laser pulse is characterized with the frequency  $\omega_0 = 2\pi c/\lambda_0$ , where  $\lambda_0$  is its vacuum wavelength. The driver is Gaussian in both spatial and temporal profiles. Its peak normalized amplitude is  $a_0 = 1.4$ . It contains a single optical cycle, i.e., its full width at half maximum duration is  $\tau_0 = 1 T_0$ , where  $T_0 = \lambda_0/c$  is the cycle period of the driver. The beam waist,  $w_0 = 4\lambda_0$ , is chosen such that the Rayleigh length of the driver is sufficiently long, and thus enables one to capture the periodic nature of the wakefield polarity reversal.

The driver, being linearly polarized along the  $z$  axis, propagates along the  $x$  axis in a preionized homogeneous slab of a hydrogen plasma with electron and proton densities  $n_{e,p} = 0.1n_c$ . The number of quasiparticles per cell is 4 for both particle species. The impact of the wakefield polarity reversal on the electron acceleration is studied using a beam of test electrons introduced through the left simulation boundary. The test electrons are initially monoenergetic with the Lorentz factor  $\gamma_e = \sqrt{10}$ , so that their velocity is comparable to the wake wave phase velocity (to fulfill the injection conditions).

The size of the simulation domain is  $120\lambda_0$  in the laser propagation direction and  $40\lambda_0$  in the transverse directions. The Cartesian grid is uniform with the resolution of 40 and 20 cells per  $\lambda_0$  along the laser propagation direction and the transverse directions, respectively. The group velocity of the driving pulse in plasma can be roughly estimated as  $v_g \simeq c\sqrt{1 - \omega_p^2/\omega_0^2} \simeq 0.95c$  and the wave number equals  $k_c = \sqrt{\omega_0^2 - \omega_p^2}/c \simeq 5.96\lambda_0^{-1}$ . This yields  $L_{\text{pr}} \simeq 2.37\lambda_0$  and  $L_d \simeq 29.24\lambda_0$  for the polarity reversal and dephasing lengths defined by Eqs. (9) and (10), respectively.

##### B. Simulation results

Figure 4 shows the temporal evolution of the wakefield on the laser propagation axis, where one may clearly see that the wakefield polarity periodically reverses [panel (a)] as well as the detail of the wakefield polarity reversal [panel (b)]. The results of the PIC simulation qualitatively correspond to the analytical model derived above (compare with Fig. 1). Figure 5 shows the spatial distribution of the wakefield at time  $t = 100T_0$ , where one may see that the polarity reversal of the wakefield occurs only in the vicinity of the laser propagation axis.

The polarity reversal length, determined by measuring the range between two longitudinal coordinates at which

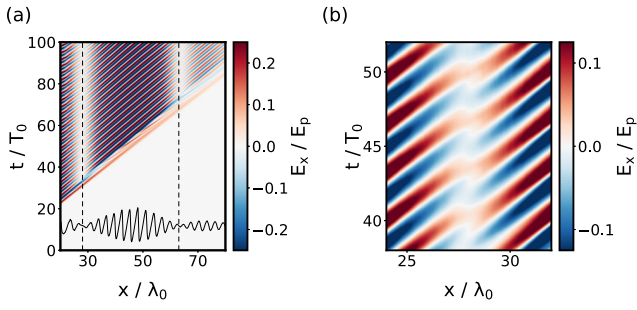


FIG. 4. Temporal evolution of the wakefield,  $E_x$ , on the laser propagation axis obtained from the 3D PIC simulation. Panel (a) shows the periodic reversal of the wakefield polarity with  $L_{pr} \approx 35\lambda_0$  (marked by dashed lines); the detail of the wakefield polarity reversal is shown in (b). The solid line at the bottom of (a) shows the line-out of the wakefield along the axis  $t = 100T_0$ .

the wakefield polarity reverses, is  $L_{pr} \approx 35\lambda_0$ . We note that the value of  $L_{pr}$  as observed in the simulation differs from the analytical prediction. This could be due to several reasons: (i) the analytical model is 1D; (ii) the driver pulse amplitude is larger than unity and thus the interaction is not in the linear regime; (iii) although the driver pulse initially consists of a single optical cycle, it is not infinitely short. Moreover, it rapidly evolves into multiple cycles during the propagation in plasma due to the dispersion.

In Fig. 6, one can see the phase space of the test electrons, the on-axis wakefield, and the on-axis driver electric field at four successive instants of time. After traversing the plane of the wakefield polarity reversal, the electrons initially located in the accelerating phase of the wakefield start to decelerate (and vice versa). This leads to significant changes in the electron energies. As can be seen from the corresponding energy spectra, the energy of electrons initially located on the top of the phase space separatrix increases by  $\approx 15\%$ .

The presented simulation indicates that, in the nonlinear regime, there may exist a case for which  $L_{pr} \approx L_d$ . In such a case, the dephasing limit is overcome and the electrons are accelerated until the energy of the driver pulse fully depletes.

## V. CONCLUSION

In conclusion, we reveal the properties of the wakefield driven by an ultrashort laser pulse in high-density plasma. The analytical model and PIC simulation show that the wakefield under the considered conditions periodically reverses its po-

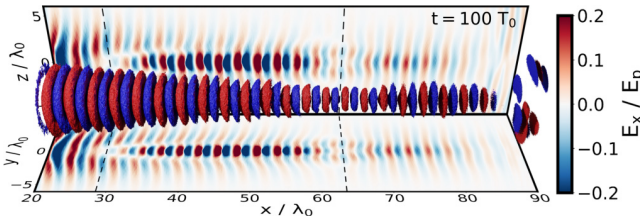


FIG. 5. Spatial distribution of the wakefield,  $E_x$ , at time  $t = 100T_0$  obtained from the 3D PIC simulation. The dashed lines indicate the periodic reversal of the wakefield polarity with  $L_{pr} \approx 35\lambda_0$ .

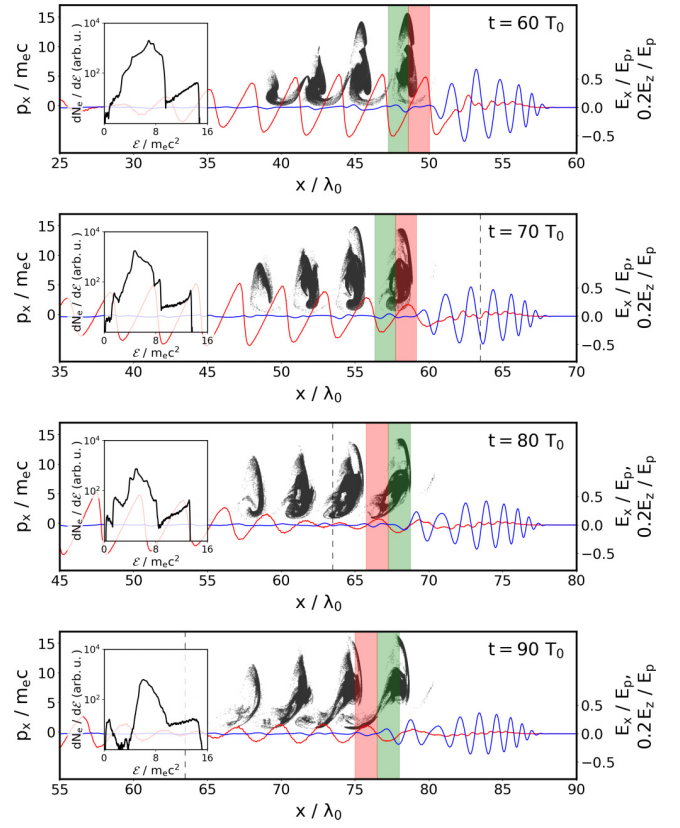


FIG. 6.  $(x, p_x)$  phase space of the test electrons (black), the on-axis wakefield,  $E_x$  (red), and the on-axis driver electric field,  $E_p$  (blue), at four successive time instants of the 3D PIC simulation. The corresponding inset shows the energy spectrum of electrons located in the first wake wave bucket behind the driver pulse, where  $N_e$  stands for the number of test electron quasiparticles. For the first wake wave bucket, the accelerating and decelerating phases of the wakefield are highlighted by green and red stripes, respectively. The longitudinal coordinate at which the wakefield polarity reversal occurs is marked by the dashed line.

larity. This phenomenon is caused by the effects of dispersion and the CEP shift of the driver which are otherwise negligible in the case of a long pulse and relatively low-density plasma. The wakefield polarity reversal occurs on spatial scales shorter than the dephasing length and, therefore, significantly affects the energies of accelerated electrons. The study presented in this work is important for the LWFA under the conditions relevant to present-day high-repetition-rate lasers, where the results obtained are useful for better controlling of the parameters of accelerated electron beams (e.g., by adjusting the initial phase of the driver or by controlling the phase of the electron injection). We note that the described wake wave structure in high-density plasma could be observed in experiments by a new generation of laboratory diagnostics [29–31].

## ACKNOWLEDGMENTS

We appreciate discussions with Prof. H. Milchberg. This work was supported by the projects “High Field Initiative” (Grant No. CZ.02.1.01/0.0/0.0/15\_003/0000449)

from the European Regional Development Fund and “IT4Innovations National Supercomputing Center” (Grant No. LM2015070) from the Ministry of Education, Youth and Sports of the Czech Republic. The EPOCH code

was in part funded by the UK Engineering and Physical Sciences Research Council (EPSRC) Grants No. EP/G054950/1, No. EP/G056803/1, No. EP/G055165/1, and No. EP/M022463/1.

- 
- [1] T. Tajima and J. M. Dawson, *Phys. Rev. Lett.* **43**, 267 (1979).
  - [2] E. Esarey, C. B. Schroeder, and W. P. Leemans, *Rev. Mod. Phys.* **81**, 1229 (2009).
  - [3] H. T. Kim, K. H. Pae, H. J. Cha, I. J. Kim, T. J. Yu, J. H. Sung, S. K. Lee, T. M. Jeong, and J. Lee, *Phys. Rev. Lett.* **111**, 165002 (2013).
  - [4] A. J. Gonsalves, K. Nakamura, J. Daniels, C. Benedetti, C. Pieronek, T. C. H. de Raadt, S. Steinke, J. H. Bin, S. S. Bulanov, J. van Tilborg, C. G. R. Geddes, C. B. Schroeder, C. Tóth, E. Esarey, K. Swanson, L. Fan-Chiang, G. Bagdasarov, N. Bobrova, V. Gasilov, G. Korn, P. Sasorov, and W. P. Leemans, *Phys. Rev. Lett.* **122**, 084801 (2019).
  - [5] J. van Tilborg, C. B. Schroeder, C. V. Filip, C. Tóth, C. G. R. Geddes, G. Fubiani, R. Huber, R. A. Kaindl, E. Esarey, and W. P. Leemans, *Phys. Rev. Lett.* **96**, 014801 (2006).
  - [6] T. Ohkubo, A. Maekawa, R. Tsujii, T. Hosokai, K. Kinoshita, K. Kobayashi, M. Uesaka, A. Zhidkov, K. Nemoto, Y. Kondo, and Y. Shibata, *Phys. Rev. ST Accel. Beams* **10**, 031301 (2007).
  - [7] A. D. Debus, M. Bussmann, U. Schramm, R. Sauerbrey, C. D. Murphy, Z. Major, R. Hörlein, L. Veisz, K. Schmid, J. Schreiber, K. Witte, S. P. Jamison, J. G. Gallacher, D. A. Jaroszynski, M. C. Kaluza, B. Hidding, S. Kiselev, R. Heathcote, P. S. Foster, D. Neely, E. J. Divall, C. J. Hooker, J. M. Smith, K. Ertel, A. J. Langley, P. Norreys, J. L. Collier, and S. Karsch, *Phys. Rev. Lett.* **104**, 084802 (2010).
  - [8] O. Lundh, J. Lim, C. Rechatin, L. Ammoura, A. Ben-Ismaïl, X. Davoine, G. Gallot, J. P. Goddet, E. Lefebvre, V. Malka, and J. Faure, *Nat. Phys.* **7**, 219 (2011).
  - [9] Y. F. Li, D. Z. Li, K. Huang, M. Z. Tao, M. H. Li, J. R. Zhao, Y. Ma, X. Guo, J. G. Wang, M. Chen, N. Hafz, J. Zhang, and L. M. Chen, *Phys. Plasmas* **24**, 023108 (2017).
  - [10] J. P. Couperus, R. Pausch, A. Köhler, O. Zarini, J. M. Krämer, M. Garten, A. Huebl, R. Gebhardt, U. Helbig, S. Bock, K. Zeil, A. Debus, M. Bussmann, U. Schramm, and A. Irman, *Nat. Commun.* **8**, 487 (2017).
  - [11] Y. Glinec, J. Faure, L. Le Dain, S. Darbon, T. Hosokai, J. J. Santos, E. Lefebvre, J. P. Rousseau, F. Burgy, B. Mercier, and V. Malka, *Phys. Rev. Lett.* **94**, 025003 (2005).
  - [12] V. Malka, J. Faure, and Y. A. Gauduel, *Mutat. Res. - Reviews Mutat. Res.* **704**, 142 (2010).
  - [13] Y. A. Gauduel, Y. Glinec, J. P. Rousseau, F. Burgy, and V. Malka, *Eur. Phys. J. D* **60**, 121 (2010).
  - [14] J. Faure, D. Gustas, D. Guénot, A. Vernier, F. Böhle, M. Ouillé, S. Haessler, R. Lopez-Martens, and A. Lifschitz, *Plasma Phys. Controlled Fusion* **61**, 014012 (2019).
  - [15] G. Sciaiani and R. J. Miller, *Rep. Prog. Phys.* **74**, 096101 (2011).
  - [16] R. J. Miller, *Science* **343**, 1108 (2014).
  - [17] K. Ta Phuoc, S. Corde, C. Thaury, V. Malka, A. Tafzi, J. P. Goddet, R. C. Shah, S. Sebban, and A. Rousse, *Nat. Photon.* **6**, 308 (2012).
  - [18] S. Corde, K. Ta Phuoc, G. Lambert, R. Fitour, V. Malka, A. Rousse, A. Beck, and E. Lefebvre, *Rev. Mod. Phys.* **85**, 1 (2013).
  - [19] Y. Muroya, M. Lin, Z. Han, Y. Kumagai, A. Sakumi, T. Ueda, and Y. Katsumura, *Radiat. Phys. Chem.* **77**, 1176 (2008).
  - [20] F. Salehi, A. J. Goers, L. Feder, B. Miao, D. Woodbury, and H. M. Milchberg, *Rev. Sci. Instrum.* **90**, 103001 (2019).
  - [21] G. Mourou, Z. Chang, A. Maksimchuk, J. Nees, S. V. Bulanov, V. Y. Bychenkov, T. Z. Esirkepov, N. M. Naumova, F. Pegoraro, and H. Ruhl, *Plasma Phys. Rep.* **28**, 12 (2002).
  - [22] Z. H. He, B. Hou, J. A. Nees, J. H. Easter, J. Faure, K. Krushelnick, and A. G. Thomas, *New J. Phys.* **15**, 053016 (2013).
  - [23] F. Salehi, A. J. Goers, G. A. Hine, L. Feder, D. Kuk, B. Miao, D. Woodbury, K. Y. Kim, and H. M. Milchberg, *Opt. Lett.* **42**, 215 (2017).
  - [24] D. Guénot, D. Gustas, A. Vernier, B. Beaurepaire, F. Böhle, M. Bocoum, M. Lozano, A. Jullien, R. Lopez-Martens, A. Lifschitz, and J. Faure, *Nat. Photon.* **11**, 293 (2017).
  - [25] E. N. Nerush and I. Y. Kostyukov, *Phys. Rev. Lett.* **103**, 035001 (2009).
  - [26] A. F. Lifschitz and V. Malka, *New J. Phys.* **14**, 053045 (2012).
  - [27] M. Ouillé, A. Vernier, F. Böhle, M. Bocoum, A. Jullien, M. Lozano, J. P. Rousseau, Z. Cheng, D. Gustas, A. Blumenstein, P. Simon, S. Haessler, J. Faure, T. Nagy, and R. Lopez-Martens, *Light: Sci. Appl.* **9**, 47 (2020).
  - [28] T. D. Arber, K. Bennett, C. S. Brady, A. Lawrence-Douglas, M. G. Ramsay, N. J. Sircombe, P. Gillies, R. G. Evans, H. Schmitz, A. R. Bell, and C. P. Ridgers, *Plasma Phys. Controlled Fusion* **57**, 113001 (2015).
  - [29] N. H. Matlis, S. Reed, S. S. Bulanov, V. Chvykov, G. Kalintchenko, T. Matsuoka, P. Rousseau, V. Yanovsky, A. Maksimchuk, S. Kalmykov, G. Shvets, and M. C. Downer, *Nat. Phys.* **2**, 749 (2006).
  - [30] M. C. Downer, R. Zgadzaj, A. Debus, U. Schramm, and M. C. Kaluza, *Rev. Mod. Phys.* **90**, 035002 (2018).
  - [31] T. Z. Esirkepov, J. Mu, Y. Gu, T. M. Jeong, P. Valenta, O. Klimo, J. Koga, M. Kando, D. Neely, G. Korn, S. V. Bulanov, and A. S. Pirozhkov, *Phys. Plasmas* **27**, 052103 (2020).



## A.2 Polarity reversal of wakefields driven by ultrashort pulse laser



## Polarity reversal of wakefields driven by ultrashort pulse laser

P. Valenta<sup>1,2,\*</sup>, T. Zh. Esirkepov<sup>1,3</sup>, J. K. Koga<sup>1,3</sup>, A. Nečas<sup>4</sup>, G. M. Grittani<sup>1</sup>, C. M. Lazzarini<sup>1</sup>, O. Klimo<sup>1,2</sup>, G. Korn<sup>1</sup>, and S. V. Bulanov<sup>1,3</sup>

<sup>1</sup>ELI Beamlines, Institute of Physics of the Czech Academy of Sciences, Na Slovance 2, Prague 18221, Czech Republic

<sup>2</sup>Faculty of Nuclear Sciences and Physical Engineering, Czech Technical University in Prague, Brehova 7, Prague 11519, Czech Republic

<sup>3</sup>Kansai Photon Science Institute, National Institutes for Quantum and Radiological Science and Technology, Umemidai 8-1-7, Kizugawa, Kyoto 619-0215, Japan

<sup>4</sup>TAE Technologies, Pauling 19631, Foothill Ranch, California 92610, USA



(Received 7 July 2020; revised 3 September 2020; accepted 25 October 2020; published 30 November 2020)

Using an analytical model and computer simulation, we show that the wakefield driven by an ultrashort laser pulse in high-density plasma periodically reverses its polarity due to the carrier-envelope phase shift of the driver. The wakefield polarity reversal occurs on spatial scales shorter than the typical length considered for electron acceleration with the laser-wakefield mechanism. Consequently, the energies of accelerated electrons are significantly affected. The results obtained are important for the laser-wakefield acceleration under the conditions relevant to present-day high-repetition-rate laser systems.

DOI: [10.1103/PhysRevE.102.053216](https://doi.org/10.1103/PhysRevE.102.053216)

### I. INTRODUCTION

Laser-wakefield acceleration (LWFA) is a well-established technique for producing high-energy electrons in plasma [1,2]. Over the past few decades, the quality of electron beams accelerated via LWFA has rapidly evolved mainly due to the advances in technology and better understanding of the underlying physics. As of 2020, LWFA has demonstrated (although not simultaneously) the capability to produce electron beams at the multi-GeV energy scale with a relative energy spread of a few percent [3,4], a few fs duration [5–8], and hundreds of pC of charge [9,10]. These achievements make LWFA increasingly attractive for a wide range of multidisciplinary experiments and applications (e.g., radiography [11], radiotherapy [12], and radiolysis [12,13]).

Recently, there has been a growing interest in LWFA driven by high-repetition-rate ( $\gtrsim$ kHz) laser systems since they can significantly improve certain characteristics (e.g., stability, signal-to-noise ratio, and average electron current [14]) required by a number of practical applications (e.g., ultrafast electron diffraction [15,16], fs x-ray generation [17,18], and pulsed radiolysis [19]). In order to produce high-quality relativistic LWFA electron sources with present-day kHz lasers, one should use tightly focused, near-single-cycle pulses and thin, near-critical density gas targets [14,20]. Such considerations constitute a great challenge not only from a technical point of view, but also in the sense of the understanding of underlying physical processes (e.g., related to the  $\lambda^3$  regime [21]).

The LWFA of electrons at kHz using laser pulses with energies  $<10$  mJ has been pursued by several groups [22–24]. The specificities of the corresponding laser-plasma

interaction, particularly the effects of the driver carrier-envelope phase (CEP) on the electron beam dynamics [25], the electron injection [26], and the electron energy spectra [14,27], were investigated. In this paper, we present the results of analytical and numerical study of the wakefield driven by an ultrashort laser pulse in high-density plasma. We show that the wakefield polarity periodically reverses due to the CEP shift of the driving pulse which significantly affects the energies of electrons accelerated via LWFA under the conditions relevant to current high-repetition-rate lasers.

### II. DISPERSION AND CARRIER-ENVELOPE PHASE SHIFT EFFECTS

The propagation of a small amplitude electromagnetic wave in collisionless plasma is governed by the dispersion equation  $\omega^2 = 1 + k^2$ . The frequency,  $\omega$ , and wave number,  $k$ , of the electromagnetic wave are measured in the units of  $\omega_p$  and  $\omega_p/c$ , respectively, where  $\omega_p = \sqrt{4\pi n_0 e^2/m_e}$  is the Langmuir frequency,  $c$  is the speed of light in vacuum,  $n_0$  is the ambient electron number density,  $e$  is the elementary charge, and  $m_e$  is the electron mass. The phase and group velocities of the electromagnetic wave (in the units of  $c$ ) are equal to  $\beta_{ph} = \sqrt{1 + k^2}/k$  and  $\beta_g = k/\sqrt{1 + k^2}$ , respectively. As one may see,  $\beta_{ph}\beta_g = 1$ .

In dispersive media, the phase and group velocities are not equal to each other,  $\beta_{ph} \neq \beta_g$ , which causes the evolution of the driver CEP. The characteristic time scale of the CEP shift effects can be expressed by a typical dispersion time,  $t_{disp}$ , defined as the time span needed to acquire the CEP shift of the driver equal to  $\pi$ ,

$$t_{disp} = \pi/\omega(\beta_{ph} - \beta_g) = \pi\beta_g/\omega(1 - \beta_g^2). \quad (1)$$

The driver field during the time interval  $<t_{disp}$  can be in one-dimensional (1D) geometry approximated by the vector

\*petr.valenta@eli-beams.eu

potential of the following form:

$$a = a_0 \frac{\sin [\Delta k(x - \beta_g t)]}{\Delta k(x - \beta_g t)} \cos [k_c(x - \beta_{\text{ph}} t) + \varphi]. \quad (2)$$

Here,  $a_0$  is the peak vacuum amplitude of the driver normalized by  $m_e c^2/e$  and  $\varphi$  is the phase of the carrier wave. The driver wave numbers are assumed to lie within a finite band  $k_c - \Delta k < k < k_c + \Delta k$ , with  $\Delta k \ll k_c$ . The spatial coordinate,  $x$ , and time,  $t$ , are measured in units of  $c/\omega_p$  and  $\omega_p^{-1}$ , respectively.

While propagating in plasma, the driver excites a wakefield that can be described by the following system of equations [2]:

$$\partial_t p + v \partial_x p = -E + F, \quad (3)$$

$$\partial_t E + v \partial_x E = v. \quad (4)$$

Here  $p$  is the  $x$  component of the electron momentum normalized by  $m_e c$ ,  $E$  is the  $x$  component of the electric field normalized by  $E_p = m_e \omega_p c/e$ , and  $v = p/\gamma$  with  $\gamma$  being the electron Lorentz factor. This yields

$$F = -(1/2\gamma) \partial_x a^2 \quad (5)$$

for the driving force (in the units of  $m_e \omega_p c$ ) with  $a(x, t)$  given by Eq. (2). The transverse component of the generalized momentum is conserved (i.e.,  $p_\perp - a = \text{const}$ ) and, therefore,  $\gamma = \sqrt{1 + a^2 + p^2}$ . In the following, we assume that  $\gamma = 1$  (i.e., the laser-plasma interaction regime is well below the wake wave breaking threshold). The nonlinear case is addressed by numerical simulation in the second part of the paper.

The system of Eqs. (3) and (4) can be solved, e.g., using Lagrange coordinates,  $x_0$  and  $\tau$ . The relation between the Euler and Langrange coordinates is defined as  $t = \tau$  and  $x = x_0 + \xi(x_0, \tau)$ , where  $x_0$  is the initial coordinate of the fluid element (at  $t = 0$ ) and  $\xi$  is a displacement of the fluid element from its initial position,  $x_0$ , to the point  $x$  during the time  $t$ ; thus  $\partial_\tau \xi = v$ . Assuming that  $\xi \ll x_0$ , the solution in quadratures reads

$$p + iE = \int_0^\tau \frac{a_0^2 k_c}{2} e^{i(\tau-\tau')} \left( \frac{\sin [\Delta k(x_0 - \beta_g \tau')]}{\Delta k(x_0 - \beta_g \tau')} \right)^2 \times \sin [2k_c(x_0 - \beta_g^{-1} \tau') + 2\varphi] d\tau'. \quad (6)$$

In the ultrashort driver pulse limit, the solution (being transformed back to the Euler coordinates) becomes

$$p = -\frac{a_0^2}{2\beta_g} \frac{k_c}{\Delta k} \cos \left( \frac{x - \beta_g t}{\beta_g} \right) \sin \left( 2k_c \frac{1 - \beta_g^2}{\beta_g^2} x - 2\varphi \right), \quad (7)$$

$$E = \frac{a_0^2}{2\beta_g} \frac{k_c}{\Delta k} \sin \left( \frac{x - \beta_g t}{\beta_g} \right) \sin \left( 2k_c \frac{1 - \beta_g^2}{\beta_g^2} x - 2\varphi \right), \quad (8)$$

where  $0 < x \leq \beta_g t$  and  $t \geq 0$ .

As can be seen from Eqs. (7) and (8), the ultrashort driver pulse in plasma excites the wakefield of a wavelength  $\lambda_w = 2\pi\beta_g$  propagating with the phase velocity,  $\beta_w$ , equal to the group velocity of the driver,  $\beta_w = \beta_g$ . In addition to the standard model, the wakefield contains a sinusoidal modulation of the amplitude due to the slippage of the driver CEP. The

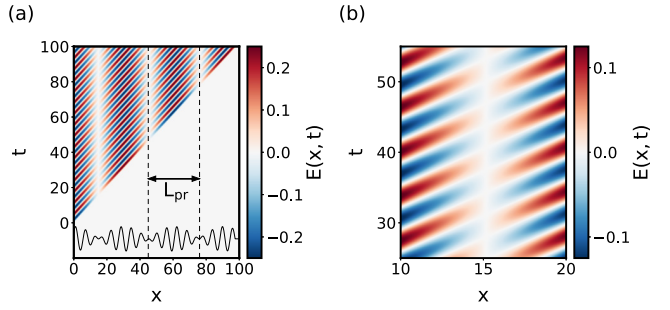


FIG. 1. Wakefield,  $E(x, t)$ , distribution in the  $(x, t)$  plane according to Eq. (8). The parameters of the driver are  $\beta_g = 0.975$ ,  $a_0 = 0.5$ ,  $k_c = 1$ ,  $\Delta k = 0.5$ , and  $\varphi = 3\pi/4$  and the plasma is homogeneous with  $n_0 = 0.5n_c$ . Panel (a) shows the periodic reversal of the wakefield polarity with  $L_{\text{pr}} \simeq 30.24$  (marked by dashed lines); the detail of the wakefield polarity reversal is shown in (b). The solid line at the bottom of (a) shows the line-out of the wakefield along the axis  $t = 100$ .

modulation wavelength, given by  $\lambda_{\text{mod}} = \pi \beta_g^2/k_c(1 - \beta_g^2)$ , corresponds to the propagation length of the driver required to shift its CEP by the factor of  $\pi$  [compare with Eq. (1)]. As a consequence, the wakefield polarity periodically reverses. The range between two adjacent longitudinal coordinates at which the wakefield polarity reversal occurs is expressed by the polarity reversal length,

$$L_{\text{pr}} = \lambda_{\text{mod}}/2 = \pi \beta_g^2/2k_c(1 - \beta_g^2). \quad (9)$$

Figure 1 shows the wakefield distribution in the  $(x, t)$  plane according to Eq. (8). The parameters of the driver are  $\beta_g = 0.975$ ,  $a_0 = 0.5$ ,  $k_c = 1$ ,  $\Delta k = 0.5$ , and  $\varphi = 3\pi/4$  and the plasma is homogeneous with  $n_0 = 0.5n_c$ , where  $n_c = n_0 \omega^2$  stands for the critical plasma density. In panel (a), one may see the periodic reversal of the wakefield polarity with  $L_{\text{pr}} \simeq 30.24$ . Panel (b) shows the detail of the wakefield polarity reversal.

### III. ELECTRON ACCELERATION BY MODULATED WAKEFIELD

As is well known, the energy of the LWFA accelerated electron is limited by the value determined by the dephasing length,

$$L_d = \pi \beta_g/(1 - \beta_g). \quad (10)$$

Following from the model, the polarity reversal length is (in underdense plasma) always shorter than the dephasing length,  $L_{\text{pr}} < L_d$ . A comparison between  $L_{\text{pr}}$  and  $L_d$  defined by Eqs. (9) and (10), respectively, is shown in Fig. 2.

The wakefield polarity reversal in its turn affects the energy of the accelerated electron. For illustration, let us consider a relativistic electron traversing the wakefield with velocity approaching the speed of light. The net change of the kinetic energy of the electron moving along the path from  $x_0 = 0$  to

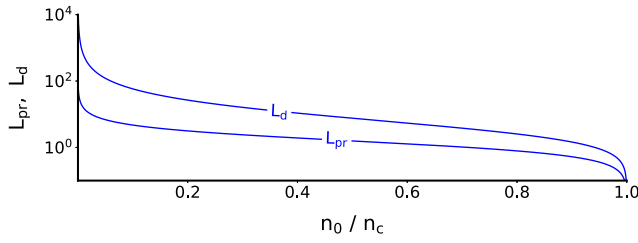


FIG. 2. Comparison between the polarity reversal length,  $L_{\text{pr}}$ , and the dephasing length,  $L_d$ , defined by Eqs. (9) and (10), respectively, in the whole range of underdense plasma.

$x_1 = x$  (in the units of  $m_e c^2$ ) is given by

$$\begin{aligned} \Delta\mathcal{E}(x) &= \int_0^x E(x', t = x') dx' \\ &= \frac{a_0^2}{4\beta_g} \frac{k_c}{\Delta k} \frac{\cos(\alpha^- x + 2\varphi) \sin(\alpha^- x)}{\alpha^-} \\ &\quad - \frac{a_0^2}{4\beta_g} \frac{k_c}{\Delta k} \frac{\cos(\alpha^+ x - 2\varphi) \sin(\alpha^+ x)}{\alpha^+}, \end{aligned} \quad (11)$$

with the coefficients  $\alpha^+$  and  $\alpha^-$  equal to

$$\alpha^\pm = \frac{\pi}{2} \left( \frac{1}{L_d} \pm \frac{1}{L_{\text{pr}}} \right). \quad (12)$$

The energy change of the electron described by Eq. (11) is shown in Fig. 3. The electron is traversing the wakefield given by Eq. (8) for the same parameters of the driver and plasma as in Fig. 1 (solid line). As can be seen, the electron either gains or loses energy over the distance of  $L_{\text{pr}} \approx 30.24$  due to the periodic reversal of the wakefield polarity. The energy balance of the electron over  $L_d \approx 122.52$  is  $\Delta\mathcal{E} \approx -1.29$ . Using the standard model (i.e., neglecting the wakefield polarity reversal), the electron would theoretically gain the energy of  $\Delta\mathcal{E} \approx 20$  over the same distance. Since  $L_{\text{pr}} \ll L_d$ , the electron energy gain under the considered conditions is always lower than the maximum value determined by the standard model.

It follows from Eq. (11) that the energy gain depends on the initial phase of the driver,  $\varphi$ . Therefore, one may find (by examining the function extrema) an optimal phase of the driver,  $\varphi_{\text{opt}}$ , for which the net energy acquired by the electron over given distance is maximal. Provided that the electron injection is localized at  $x = 0$  and the acceleration takes place

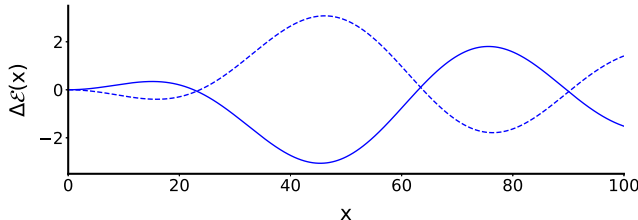


FIG. 3. Energy change of the relativistic electron,  $\Delta\mathcal{E}(x)$ , according to Eq. (11). The solid line shows the energy change of electron traversing the wakefield described by Eq. (8) for the same parameters of the driver and plasma as in Fig. 1. The dashed line shows the energy change of electron for  $\varphi = \varphi_{\text{opt}}$ .

over  $L_d$ ,

$$\varphi_{\text{opt}}^n = \frac{\pi}{4} \left( 1 + \frac{L_d}{L_{\text{pr}}} \right) + n\pi, \quad n \in \mathbb{Z}. \quad (13)$$

The energy change of the electron for  $\varphi = \varphi_{\text{opt}}$  is shown in Fig. 3 by the dashed line.

#### IV. PARTICLE-IN-CELL SIMULATION

##### A. Simulation setup

Now we explore the self-consistent evolution of the ultra-short laser pulse and near-critical density plasma numerically by means of particle-in-cell (PIC) simulation in a three-dimensional (3D) Cartesian geometry. The simulation is carried out using the PIC code EPOCH [28]. The driver laser pulse is characterized with the frequency  $\omega_0 = 2\pi c/\lambda_0$ , where  $\lambda_0$  is its vacuum wavelength. The driver is Gaussian in both spatial and temporal profiles. Its peak normalized amplitude is  $a_0 = 1.4$ . It contains a single optical cycle, i.e., its full width at half maximum duration is  $\tau_0 = 1 T_0$ , where  $T_0 = \lambda_0/c$  is the cycle period of the driver. The beam waist,  $w_0 = 4\lambda_0$ , is chosen such that the Rayleigh length of the driver is sufficiently long, and thus enables one to capture the periodic nature of the wakefield polarity reversal.

The driver, being linearly polarized along the  $z$  axis, propagates along the  $x$  axis in a preionized homogeneous slab of a hydrogen plasma with electron and proton densities  $n_{e,p} = 0.1n_c$ . The number of quasiparticles per cell is 4 for both particle species. The impact of the wakefield polarity reversal on the electron acceleration is studied using a beam of test electrons introduced through the left simulation boundary. The test electrons are initially monoenergetic with the Lorentz factor  $\gamma_e = \sqrt{10}$ , so that their velocity is comparable to the wake wave phase velocity (to fulfill the injection conditions).

The size of the simulation domain is  $120\lambda_0$  in the laser propagation direction and  $40\lambda_0$  in the transverse directions. The Cartesian grid is uniform with the resolution of 40 and 20 cells per  $\lambda_0$  along the laser propagation direction and the transverse directions, respectively. The group velocity of the driving pulse in plasma can be roughly estimated as  $v_g \approx c\sqrt{1 - \omega_p^2/\omega_0^2} \approx 0.95c$  and the wave number equals  $k_c = \sqrt{\omega_0^2 - \omega_p^2}/c \approx 5.96\lambda_0^{-1}$ . This yields  $L_{\text{pr}} \approx 2.37\lambda_0$  and  $L_d \approx 29.24\lambda_0$  for the polarity reversal and dephasing lengths defined by Eqs. (9) and (10), respectively.

##### B. Simulation results

Figure 4 shows the temporal evolution of the wakefield on the laser propagation axis, where one may clearly see that the wakefield polarity periodically reverses [panel (a)] as well as the detail of the wakefield polarity reversal [panel (b)]. The results of the PIC simulation qualitatively correspond to the analytical model derived above (compare with Fig. 1). Figure 5 shows the spatial distribution of the wakefield at time  $t = 100T_0$ , where one may see that the polarity reversal of the wakefield occurs only in the vicinity of the laser propagation axis.

The polarity reversal length, determined by measuring the range between two longitudinal coordinates at which

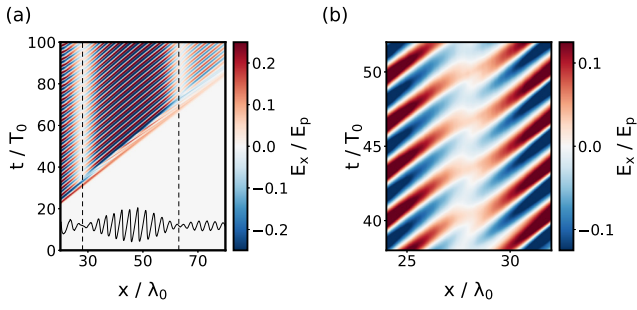


FIG. 4. Temporal evolution of the wakefield,  $E_x$ , on the laser propagation axis obtained from the 3D PIC simulation. Panel (a) shows the periodic reversal of the wakefield polarity with  $L_{pr} \approx 35\lambda_0$  (marked by dashed lines); the detail of the wakefield polarity reversal is shown in (b). The solid line at the bottom of (a) shows the line-out of the wakefield along the axis  $t = 100T_0$ .

the wakefield polarity reverses, is  $L_{pr} \approx 35\lambda_0$ . We note that the value of  $L_{pr}$  as observed in the simulation differs from the analytical prediction. This could be due to several reasons: (i) the analytical model is 1D; (ii) the driver pulse amplitude is larger than unity and thus the interaction is not in the linear regime; (iii) although the driver pulse initially consists of a single optical cycle, it is not infinitely short. Moreover, it rapidly evolves into multiple cycles during the propagation in plasma due to the dispersion.

In Fig. 6, one can see the phase space of the test electrons, the on-axis wakefield, and the on-axis driver electric field at four successive instants of time. After traversing the plane of the wakefield polarity reversal, the electrons initially located in the accelerating phase of the wakefield start to decelerate (and vice versa). This leads to significant changes in the electron energies. As can be seen from the corresponding energy spectra, the energy of electrons initially located on the top of the phase space separatrix increases by  $\approx 15\%$ .

The presented simulation indicates that, in the nonlinear regime, there may exist a case for which  $L_{pr} \approx L_d$ . In such a case, the dephasing limit is overcome and the electrons are accelerated until the energy of the driver pulse fully depletes.

## V. CONCLUSION

In conclusion, we reveal the properties of the wakefield driven by an ultrashort laser pulse in high-density plasma. The analytical model and PIC simulation show that the wakefield under the considered conditions periodically reverses its po-

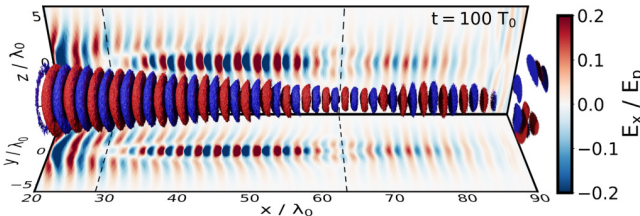


FIG. 5. Spatial distribution of the wakefield,  $E_x$ , at time  $t = 100T_0$  obtained from the 3D PIC simulation. The dashed lines indicate the periodic reversal of the wakefield polarity with  $L_{pr} \approx 35\lambda_0$ .

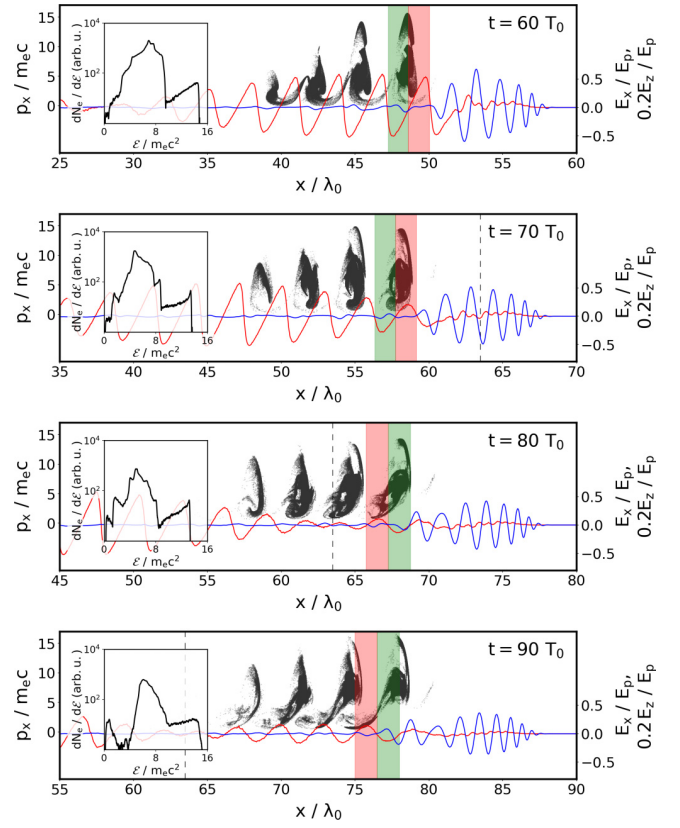


FIG. 6.  $(x, p_x)$  phase space of the test electrons (black), the on-axis wakefield,  $E_x$  (red), and the on-axis driver electric field,  $E_p$  (blue), at four successive time instants of the 3D PIC simulation. The corresponding inset shows the energy spectrum of electrons located in the first wake wave bucket behind the driver pulse, where  $N_e$  stands for the number of test electron quasiparticles. For the first wake wave bucket, the accelerating and decelerating phases of the wakefield are highlighted by green and red stripes, respectively. The longitudinal coordinate at which the wakefield polarity reversal occurs is marked by the dashed line.

larity. This phenomenon is caused by the effects of dispersion and the CEP shift of the driver which are otherwise negligible in the case of a long pulse and relatively low-density plasma. The wakefield polarity reversal occurs on spatial scales shorter than the dephasing length and, therefore, significantly affects the energies of accelerated electrons. The study presented in this work is important for the LWFA under the conditions relevant to present-day high-repetition-rate lasers, where the results obtained are useful for better controlling of the parameters of accelerated electron beams (e.g., by adjusting the initial phase of the driver or by controlling the phase of the electron injection). We note that the described wake wave structure in high-density plasma could be observed in experiments by a new generation of laboratory diagnostics [29–31].

## ACKNOWLEDGMENTS

We appreciate discussions with Prof. H. Milchberg. This work was supported by the projects “High Field Initiative” (Grant No. CZ.02.1.01/0.0/0.0/15\_003/0000449)

from the European Regional Development Fund and “IT4Innovations National Supercomputing Center” (Grant No. LM2015070) from the Ministry of Education, Youth and Sports of the Czech Republic. The EPOCH code

was in part funded by the UK Engineering and Physical Sciences Research Council (EPSRC) Grants No. EP/G054950/1, No. EP/G056803/1, No. EP/G055165/1, and No. EP/M022463/1.

- 
- [1] T. Tajima and J. M. Dawson, *Phys. Rev. Lett.* **43**, 267 (1979).
  - [2] E. Esarey, C. B. Schroeder, and W. P. Leemans, *Rev. Mod. Phys.* **81**, 1229 (2009).
  - [3] H. T. Kim, K. H. Pae, H. J. Cha, I. J. Kim, T. J. Yu, J. H. Sung, S. K. Lee, T. M. Jeong, and J. Lee, *Phys. Rev. Lett.* **111**, 165002 (2013).
  - [4] A. J. Gonsalves, K. Nakamura, J. Daniels, C. Benedetti, C. Pieronek, T. C. H. de Raadt, S. Steinke, J. H. Bin, S. S. Bulanov, J. van Tilborg, C. G. R. Geddes, C. B. Schroeder, C. Tóth, E. Esarey, K. Swanson, L. Fan-Chiang, G. Bagdasarov, N. Bobrova, V. Gasilov, G. Korn, P. Sasorov, and W. P. Leemans, *Phys. Rev. Lett.* **122**, 084801 (2019).
  - [5] J. van Tilborg, C. B. Schroeder, C. V. Filip, C. Tóth, C. G. R. Geddes, G. Fubiani, R. Huber, R. A. Kaindl, E. Esarey, and W. P. Leemans, *Phys. Rev. Lett.* **96**, 014801 (2006).
  - [6] T. Ohkubo, A. Maekawa, R. Tsujii, T. Hosokai, K. Kinoshita, K. Kobayashi, M. Uesaka, A. Zhidkov, K. Nemoto, Y. Kondo, and Y. Shibata, *Phys. Rev. ST Accel. Beams* **10**, 031301 (2007).
  - [7] A. D. Debus, M. Bussmann, U. Schramm, R. Sauerbrey, C. D. Murphy, Z. Major, R. Hörlein, L. Veisz, K. Schmid, J. Schreiber, K. Witte, S. P. Jamison, J. G. Gallacher, D. A. Jaroszynski, M. C. Kaluza, B. Hidding, S. Kiselev, R. Heathcote, P. S. Foster, D. Neely, E. J. Divall, C. J. Hooker, J. M. Smith, K. Ertel, A. J. Langley, P. Norreys, J. L. Collier, and S. Karsch, *Phys. Rev. Lett.* **104**, 084802 (2010).
  - [8] O. Lundh, J. Lim, C. Rechatin, L. Ammoura, A. Ben-Ismaïl, X. Davoine, G. Gallot, J. P. Goddet, E. Lefebvre, V. Malka, and J. Faure, *Nat. Phys.* **7**, 219 (2011).
  - [9] Y. F. Li, D. Z. Li, K. Huang, M. Z. Tao, M. H. Li, J. R. Zhao, Y. Ma, X. Guo, J. G. Wang, M. Chen, N. Hafz, J. Zhang, and L. M. Chen, *Phys. Plasmas* **24**, 023108 (2017).
  - [10] J. P. Couperus, R. Pausch, A. Köhler, O. Zarini, J. M. Krämer, M. Garten, A. Huebl, R. Gebhardt, U. Helbig, S. Bock, K. Zeil, A. Debus, M. Bussmann, U. Schramm, and A. Irman, *Nat. Commun.* **8**, 487 (2017).
  - [11] Y. Glinec, J. Faure, L. Le Dain, S. Darbon, T. Hosokai, J. J. Santos, E. Lefebvre, J. P. Rousseau, F. Burgy, B. Mercier, and V. Malka, *Phys. Rev. Lett.* **94**, 025003 (2005).
  - [12] V. Malka, J. Faure, and Y. A. Gauduel, *Mutat. Res. - Reviews Mutat. Res.* **704**, 142 (2010).
  - [13] Y. A. Gauduel, Y. Glinec, J. P. Rousseau, F. Burgy, and V. Malka, *Eur. Phys. J. D* **60**, 121 (2010).
  - [14] J. Faure, D. Gustas, D. Guénot, A. Vernier, F. Böhle, M. Ouillé, S. Haessler, R. Lopez-Martens, and A. Lifschitz, *Plasma Phys. Controlled Fusion* **61**, 014012 (2019).
  - [15] G. Sciaiani and R. J. Miller, *Rep. Prog. Phys.* **74**, 096101 (2011).
  - [16] R. J. Miller, *Science* **343**, 1108 (2014).
  - [17] K. Ta Phuoc, S. Corde, C. Thaury, V. Malka, A. Tafzi, J. P. Goddet, R. C. Shah, S. Sebban, and A. Rousse, *Nat. Photon.* **6**, 308 (2012).
  - [18] S. Corde, K. Ta Phuoc, G. Lambert, R. Fitour, V. Malka, A. Rousse, A. Beck, and E. Lefebvre, *Rev. Mod. Phys.* **85**, 1 (2013).
  - [19] Y. Muroya, M. Lin, Z. Han, Y. Kumagai, A. Sakumi, T. Ueda, and Y. Katsumura, *Radiat. Phys. Chem.* **77**, 1176 (2008).
  - [20] F. Salehi, A. J. Goers, L. Feder, B. Miao, D. Woodbury, and H. M. Milchberg, *Rev. Sci. Instrum.* **90**, 103001 (2019).
  - [21] G. Mourou, Z. Chang, A. Maksimchuk, J. Nees, S. V. Bulanov, V. Y. Bychenkov, T. Z. Esirkepov, N. M. Naumova, F. Pegoraro, and H. Ruhl, *Plasma Phys. Rep.* **28**, 12 (2002).
  - [22] Z. H. He, B. Hou, J. A. Nees, J. H. Easter, J. Faure, K. Krushelnick, and A. G. Thomas, *New J. Phys.* **15**, 053016 (2013).
  - [23] F. Salehi, A. J. Goers, G. A. Hine, L. Feder, D. Kuk, B. Miao, D. Woodbury, K. Y. Kim, and H. M. Milchberg, *Opt. Lett.* **42**, 215 (2017).
  - [24] D. Guénot, D. Gustas, A. Vernier, B. Beaurepaire, F. Böhle, M. Bocoum, M. Lozano, A. Jullien, R. Lopez-Martens, A. Lifschitz, and J. Faure, *Nat. Photon.* **11**, 293 (2017).
  - [25] E. N. Nerush and I. Y. Kostyukov, *Phys. Rev. Lett.* **103**, 035001 (2009).
  - [26] A. F. Lifschitz and V. Malka, *New J. Phys.* **14**, 053045 (2012).
  - [27] M. Ouillé, A. Vernier, F. Böhle, M. Bocoum, A. Jullien, M. Lozano, J. P. Rousseau, Z. Cheng, D. Gustas, A. Blumenstein, P. Simon, S. Haessler, J. Faure, T. Nagy, and R. Lopez-Martens, *Light: Sci. Appl.* **9**, 47 (2020).
  - [28] T. D. Arber, K. Bennett, C. S. Brady, A. Lawrence-Douglas, M. G. Ramsay, N. J. Sircombe, P. Gillies, R. G. Evans, H. Schmitz, A. R. Bell, and C. P. Ridgers, *Plasma Phys. Controlled Fusion* **57**, 113001 (2015).
  - [29] N. H. Matlis, S. Reed, S. S. Bulanov, V. Chvykov, G. Kalintchenko, T. Matsuoka, P. Rousseau, V. Yanovsky, A. Maksimchuk, S. Kalmykov, G. Shvets, and M. C. Downer, *Nat. Phys.* **2**, 749 (2006).
  - [30] M. C. Downer, R. Zgadzaj, A. Debus, U. Schramm, and M. C. Kaluza, *Rev. Mod. Phys.* **90**, 035002 (2018).
  - [31] T. Z. Esirkepov, J. Mu, Y. Gu, T. M. Jeong, P. Valenta, O. Klimo, J. Koga, M. Kando, D. Neely, G. Korn, S. V. Bulanov, and A. S. Pirozhkov, *Phys. Plasmas* **27**, 052103 (2020).

### A.3 Recoil effects on reflection from relativistic mirrors in laser plasmas

# Recoil effects on reflection from relativistic mirrors in laser plasmas

Cite as: Phys. Plasmas **27**, 032109 (2020); doi: 10.1063/1.5142084

Submitted: 10 December 2019 · Accepted: 21 February 2020 ·

Published Online: 10 March 2020



View Online



Export Citation



CrossMark

P. Valenta,<sup>1,2,a)</sup> T. Zh. Esirkepov,<sup>3</sup> J. K. Koga,<sup>3</sup> A. S. Pirozhkov,<sup>3</sup> M. Kando,<sup>3</sup> T. Kawachi,<sup>3</sup> Y.-K. Liu,<sup>4</sup> P. Fang,<sup>4</sup> P. Chen,<sup>4</sup> J. Mu,<sup>1</sup> G. Korn,<sup>1</sup> O. Klimo,<sup>1,2</sup> and S. V. Bulanov<sup>1,3,5</sup>

## AFFILIATIONS

<sup>1</sup>ELI Beamlines, Institute of Physics, Czech Academy of Sciences, Na Slovance 2, 18221 Prague, Czech Republic

<sup>2</sup>Faculty of Nuclear Sciences and Physical Engineering, Czech Technical University in Prague, Brehova 7, 11519 Prague, Czech Republic

<sup>3</sup>Kansai Photon Science Institute, National Institutes for Quantum and Radiological Science and Technology, Umemidai 8-1-7, Kizugawa, 619-0215 Kyoto, Japan

<sup>4</sup>Leung Center for Cosmology and Particle Astrophysics, National Taiwan University, No. 1, Sec. 4, Roosevelt Rd., 10617 Taipei, Taiwan

<sup>5</sup>Prokhorov Institute of General Physics, Russian Academy of Sciences, Vavilova 38, 119991 Moscow, Russia

<sup>a)</sup>Author to whom correspondence should be addressed: petr.valenta@eli-beams.eu

## ABSTRACT

Relativistic mirrors can be realized with strongly nonlinear Langmuir waves excited by intense laser pulses in underdense plasma. On reflection from the relativistic mirror, the incident light affects the mirror motion. The corresponding recoil effects are investigated analytically and using particle-in-cell simulations. It is found that if the fluence of the incident electromagnetic wave exceeds a certain threshold, the relativistic mirror undergoes a significant back reaction and splits into multiple electron layers. The reflection coefficient of the relativistic mirror and the factors of electric field amplification and frequency upshift of the electromagnetic wave are obtained.

Published under license by AIP Publishing. <https://doi.org/10.1063/1.5142084>

## I. INTRODUCTION

A relativistic mirror may be defined as an object that reflects incoming radiation while moving at relativistic velocity. The theory of light reflection from such an object propagating in vacuum at arbitrary (subluminal) velocity was first formulated by Einstein in 1905.<sup>1</sup> Since then, relativistic mirrors have been studied in many different contexts because of their great potential for both fundamental science and practical applications.

An electromagnetic wave incident on a relativistic mirror undergoes energy and frequency changes due to the double Doppler effect. In a co-propagating configuration in the laboratory frame of reference, the reflected wave is stretched, its amplitude is lowered, and its frequency is downshifted. In contrast, in a counter-propagating configuration, the reflected wave is compressed and amplified and its frequency is upshifted.

Relativistic mirrors can be realized by irradiating plasma targets with intense laser pulses (see Ref. 2 for a review and the literature cited therein). They appear in laser plasma as thin dense electron (or electron-ion) shells accelerated to relativistic velocities. Various schemes that lead to the generation of relativistic mirrors have been described

in theoretical and experimental studies (e.g., double-sided mirrors,<sup>3–13</sup> oscillating mirrors,<sup>14–19</sup> sliding mirrors,<sup>20,21</sup> flying mirrors realized with strongly nonlinear Langmuir waves,<sup>22–28</sup> or electron density singularities<sup>29</sup>) and, hence, have already proven the feasibility of this concept.

Nowadays, relativistic mirrors in plasmas are actively studied as a unique tool for fundamental research (e.g., light intensification toward the Schwinger limit,<sup>22</sup> investigation of photon–photon and Delbrück scattering<sup>27,30</sup> analog black hole to investigate Hawking radiation, and the information loss paradox<sup>31</sup>) and for many practical applications in diverse fields; depending on whether the configuration is co-propagating or counter-propagating in the laboratory frame of reference, relativistic mirrors might be used either for the acceleration of ions (e.g., for hadron therapy<sup>32</sup>) or for producing coherent high-brightness radiation with wavelengths ranging from x-ray to gamma-ray (e.g., for molecular imaging<sup>33</sup> and attosecond spectroscopy<sup>34</sup>).

Maximization of the reflected radiation energy requires a more intense incident electromagnetic wave. However, sufficiently strong incident light can significantly affect the motion of the relativistic mirror (i.e., its radiation pressure can stop or destroy the mirror). In the

present paper, we aim at a closer description of the recoil effects on a reflection from the relativistic mirror. We study the interaction of strongly nonlinear Langmuir waves with an incident counter-propagating electromagnetic wave and the properties of the reflected radiation. We discuss the regimes when the relativistic mirror undergoes a significant back reaction. We find the threshold of the onset of the recoil effects.

This paper is organized as follows: in Sec. II, we derive the threshold for the energy of the incident electromagnetic wave; in Sec. III, we discuss the physical realization of relativistic mirrors in laser plasma; and in Sec. IV, we demonstrate the results of one-dimensional (1D) particle-in-cell (PIC) simulations and compare them with the analytical calculations.

## II. RECOIL EFFECTS ON REFLECTION FROM RELATIVISTIC MIRRORS

For a relativistic mirror propagating at constant velocity  $v_M$  in vacuum, the frequency upshift of a normally incident counter-propagating electromagnetic wave is given by<sup>1</sup>

$$\frac{\omega}{\omega_0} = \frac{1 + \beta_M}{1 - \beta_M} = \frac{\gamma_M + \sqrt{\gamma_M^2 - 1}}{\gamma_M - \sqrt{\gamma_M^2 - 1}} \approx 4\gamma_M^2, \quad (1)$$

where  $\omega$  and  $\omega_0$  are the frequencies of the reflected and incident radiation, respectively,  $\beta_M = v_M/c$  is the velocity of the relativistic mirror normalized by the speed of light in vacuum  $c$ , and  $\gamma_M = 1/\sqrt{1 - \beta_M^2}$  is the corresponding relativistic Lorentz factor. The last term in Eq. (1) is obtained using the identity  $\gamma_M + \sqrt{\gamma_M^2 - 1} = (\gamma_M - \sqrt{\gamma_M^2 - 1})^{-1}$  and  $\gamma_M + \sqrt{\gamma_M^2 - 1} \approx 2\gamma_M$  and is valid in the ultra-relativistic limit, i.e., when  $\gamma_M \gg 1$ . The factor of the electric field amplification of the reflected wave is given by<sup>1</sup>

$$\frac{E}{E_0} = \frac{\omega}{\omega_0} \sqrt{R}, \quad (2)$$

where  $E$  and  $E_0$  are the electric fields of the reflected and incident radiation, respectively, and  $R$  stands for the reflection coefficient in terms of the photon number.

Eqs. (1) and (2) are derived in the approximation of a weak incident electromagnetic wave. Here, we analytically investigate the recoil effects of a counter-propagating electromagnetic wave normally incident on a relativistic mirror. This problem was briefly discussed in Ref. 21. First, we consider the relativistic mirror in the form of an electron layer. We assume that all the electrons are characterized by the same momentum, the electromagnetic wave is monochromatic, and the reflection coefficient in terms of the photon number is equal to  $R$ . The conservation of momentum and energy before and after the interaction can be then written as

$$\mathcal{N}_e p_{e0} - \mathcal{N}_\gamma p_{\gamma0} = \mathcal{N}_e p_e + R \mathcal{N}_\gamma p_\gamma - (1 - R) \mathcal{N}_\gamma p_{\gamma0}, \quad (3)$$

$$\mathcal{N}_e \mathcal{E}_{e0} + \mathcal{N}_\gamma E_{\gamma0} = \mathcal{N}_e \mathcal{E}_e + R \mathcal{N}_\gamma \mathcal{E}_\gamma + (1 - R) \mathcal{N}_\gamma \mathcal{E}_{\gamma0}. \quad (4)$$

Here,  $\mathcal{N}_e$  and  $\mathcal{N}_\gamma$  are the numbers of interacting electrons and photons, respectively. The subscript “0” denotes the quantities before the interaction, and the “−” sign in Eq. (3) denotes counter-propagating photons. The electron and photon momenta and energies can be expressed as

$$p_e = m_e c \sqrt{\gamma_e^2 - 1}, \quad p_\gamma = \hbar \omega / c, \quad (5)$$

$$\mathcal{E}_e = m_e c^2 \gamma_e, \quad \mathcal{E}_\gamma = \hbar \omega, \quad (6)$$

where the symbols  $\hbar$ ,  $\gamma_e$  and  $m_e$  denote the reduced Planck constant, the relativistic Lorentz factor of electrons, and the electron rest mass, respectively.

By combining Eqs. (3)–(6), we obtain the following formula:

$$\begin{aligned} \hbar \omega &= \hbar \omega_0 \frac{\mathcal{N}_e (\mathcal{E}_{e0} + p_{e0} c)}{\mathcal{N}_e (\mathcal{E}_{e0} - p_{e0} c) + 2R \mathcal{N}_\gamma \hbar \omega_0} \\ &= \hbar \omega_0 \frac{\mathcal{N}_e m_e c^2 (\gamma_{e0} + \sqrt{\gamma_{e0}^2 - 1})}{\mathcal{N}_e m_e c^2 (\gamma_{e0} - \sqrt{\gamma_{e0}^2 - 1}) + 2R \mathcal{N}_\gamma \hbar \omega_0}. \end{aligned} \quad (7)$$

In the ultrarelativistic limit, i.e., when  $\gamma_{e0} \gg 1$ , Eq. (7) can be simplified as

$$\frac{\omega}{\omega_0} \approx 4\gamma_{e0}^2 \frac{\frac{\mathcal{N}_e m_e c^2}{4\gamma_{e0}}}{\frac{\mathcal{N}_e m_e c^2}{4\gamma_{e0}} + R \mathcal{N}_\gamma \hbar \omega_0}. \quad (8)$$

The two terms in the denominator of Eq. (8) correspond to the energy of the electron layer and interacting photons, respectively. The resulting frequency upshift of the reflected radiation is determined by the relationship between both terms

$$\omega/\omega_0 \approx 4\gamma_{e0}^2 \quad \text{for} \quad R \mathcal{N}_\gamma \hbar \omega_0 \ll \frac{\mathcal{N}_e m_e c^2}{4\gamma_{e0}}, \quad (9a)$$

$$\omega/\omega_0 \approx \frac{\mathcal{N}_e m_e c^2 \gamma_{e0}}{R \mathcal{N}_\gamma \hbar \omega_0} \quad \text{for} \quad R \mathcal{N}_\gamma \hbar \omega_0 \gg \frac{\mathcal{N}_e m_e c^2}{4\gamma_{e0}}. \quad (9b)$$

The limit (9a) corresponds to the approximation of a weak incident electromagnetic wave and produces the classical frequency upshift factor corresponding to the double Doppler effect [see Eq. (1)]. In the opposite limit (9b), the incident radiation significantly affects the motion of relativistic mirror, so that the frequency of the reflected electromagnetic wave is in fact downshifted by the factor of  $\mathcal{N}_e m_e c^2 \gamma_{e0} / (R \mathcal{N}_\gamma \hbar \omega_0) \ll 1$ .

We define the threshold characterizing the recoil importance in this interaction as a midpoint between the limits given by Eqs. (9a) and (9b), when the energy of the interacting photons is comparable to that of the electron layer,

$$R \mathcal{N}_\gamma \hbar \omega_0 = \varkappa \frac{\mathcal{N}_e m_e c^2}{4\gamma_{e0}}, \quad (10)$$

where  $\varkappa < 1$  is a small factor. Obviously, much less energy than the kinetic energy of the mirror can affect the reflection process.

## III. RELATIVISTIC MIRROR REALIZED WITH A LANGMUIR WAVE

A sufficiently short and intense laser pulse excites a strongly nonlinear Langmuir wave in underdense plasma.<sup>35,36</sup> The electron density modulations of the Langmuir wave in the wake of the laser pulse take the form of thin dense shells separated by cavities of the length corresponding to the Langmuir wave wavelength  $\lambda_w$ . A weak counter-propagating electromagnetic wave is partially reflected from these

shells, undergoing energy and frequency changes in accordance with the double Doppler effect. For this case, Eq. (1) becomes<sup>2</sup>

$$\begin{aligned}\frac{\omega}{\omega_0} &= \frac{1}{1 - \beta_w^2} \left( 1 + \beta_w^2 + 2\beta_w \sqrt{1 - \frac{\omega_{pe}^2}{\omega_0^2}} \right) \\ &= 2\gamma_w^2 + 2\gamma_w \sqrt{\gamma_w^2 - 1} \sqrt{1 - \frac{\omega_{pe}^2}{\omega_0^2}} - 1\end{aligned}\quad (11)$$

so that it includes the difference between the phase and group velocity in plasma. Here,  $\omega_{pe} = \sqrt{4\pi n_e e^2 / m_e}$  is the Langmuir frequency corresponding to the background electron density  $n_e$ ,  $\beta_w$  is the phase velocity of the Langmuir wave normalized by  $c$ , and  $\gamma_w = 1 / \sqrt{1 - \beta_w^2}$  is the corresponding relativistic Lorentz factor. The symbol  $e$  stands for the elementary charge.

If the velocity of the electrons in the vicinity of the electron density spike exceeds the phase velocity of the Langmuir wave, i.e.,  $\gamma_e > \gamma_w$ , the Langmuir wave breaks. This corresponds to the Akhiezer-Polovin limit<sup>37</sup> for the longitudinal electric field,  $E_x$ , of the Langmuir wave,

$$\frac{\max|E_x|e}{m_e \omega_{pe} c} > \sqrt{2(\gamma_w - 1)}. \quad (12)$$

For the Langmuir wave at the threshold of wave-breaking, its reflection coefficient in terms of the photon number,  $R$ , is (see Ref. 2)

$$R \approx \frac{\Gamma^2(2/3)}{2^2 \cdot 3^{4/3}} \left( \frac{\omega_{pe}}{\omega_0} \right)^{8/3} \frac{1}{\gamma_w^{4/3}}, \quad (13)$$

where  $\Gamma(x)$  is the Euler gamma function.<sup>38</sup>

In order to estimate the threshold given by Eq. (10) for the relativistic mirror realized with a breaking Langmuir wave, we represent, for simplicity, the incident laser pulse as an electromagnetic wavepacket with a rectangular profile and intensity  $I$ , duration  $\tau$ , and cross-sectional area  $S$ . We assume the normal incidence of this wavepacket on the relativistic mirror. The number of photons in the pulse,  $\mathcal{N}_\gamma$ , is given by the following expression:

$$\mathcal{N}_\gamma = \frac{I\tau S}{\hbar\omega_0}. \quad (14)$$

For a nearly breaking Langmuir wave, for which Eq. (13) holds, approximately half of the plasma electrons are concentrated in the electron density spike in each wave period. Therefore, the number of interacting electrons,  $\mathcal{N}_e$ , is

$$\mathcal{N}_e = \frac{n_e}{2} \lambda_w S. \quad (15)$$

Using the reflection coefficient of the Langmuir wave of Eq. (13) and the number of interacting photons and electrons of Eqs. (14) and (15), respectively, we rewrite the threshold of Eq. (10) in terms of the fluence (the product of intensity and duration) of the incident wavepacket,

$$\begin{aligned}I\tau &= \varkappa \frac{m_e c^2}{8} \frac{n_e \lambda_w}{\gamma_w R} \\ &= \varkappa \frac{3^{4/3} m_e c^2}{2\Gamma^2(2/3)} \left( \frac{\omega_0}{\omega_{pe}} \right)^{8/3} \gamma_w^{1/3} n_e \lambda_w.\end{aligned}\quad (16)$$

As can be seen from this formula, even a low intensity electromagnetic wavepacket is able to destroy the mirror, if it is sufficiently long. However, the relativistic mirror realized with the Langmuir wave consists of electrons that are continuously flowing through it. Consequently, the structure of the electron density spike is being refreshed every moment in time. Thus, the applicability of the model given by Eqs. (3)–(6) is better for a short-time interaction and sufficiently large electromagnetic wave intensity. We interpret the threshold of Eq. (16) as a condition for the minimum wavepacket duration required for a recoil effect,

$$\tau_{\min} = \varkappa \frac{3^{4/3} m_e c^2}{2\Gamma^2(2/3)} \left( \frac{\omega_0}{\omega_{pe}} \right)^{8/3} \gamma_w^{1/3} \frac{n_e \lambda_w}{I}. \quad (17)$$

In this interpretation, the incident wavepacket intensity becomes the main critical parameter for the recoil effects. Below, we investigate the applicability of the model and, in particular, Eq. (17) by PIC simulations.

#### IV. PARTICLE-IN-CELL SIMULATIONS

The properties of relativistic mirrors realized with strongly nonlinear Langmuir waves in underdense plasmas are studied numerically by means of PIC simulations in a 1D Cartesian geometry. The 1D configuration is sufficient for the investigation of the Langmuir wave interaction with a counter-propagating laser pulse and beneficial in view of the necessity of resolving frequency upshifted electromagnetic radiation according to Eq. (11). The results can be extrapolated to higher dimensions considering laser pulses with a wide focal spot. The simulations are performed using the fully relativistic electromagnetic PIC EPOCH code.<sup>39</sup>

##### A. Simulation setup

The laser pulse that drives the Langmuir wave (from here on referred to as the “driver”) enters the simulation domain from the left boundary and propagates in the  $+x$  direction. The laser pulse that undergoes the reflection from the Langmuir wave (from here on referred to as the “source”) enters from the right and propagates in the opposite (i.e.,  $-x$ ) direction. In the following, we use the superscripts “ $d$ ”, “ $s$ ”, and “ $r$ ” to denote the quantities, which characterize the driver, the source, and the reflected pulse, respectively.

The driver is characterized by a wavelength in vacuum  $\lambda_0^d = 2\pi c / \omega_0^d$ , where  $\omega_0^d$  is its angular frequency, and by the normalized amplitude  $a_0^d = 10$  defined as  $a_0^d = eE_0^d / (m_e \omega_0^d c)$ , where  $E_0^d$  is the amplitude of the electric field in vacuum. Its temporal profile is Gaussian with a full-width-at-half-maximum duration  $\tau_0^d = 10 T_0^d$ , where  $T_0^d = \lambda_0^d / c$  is the driver pulse cycle period. The values of  $a_0^d$  and  $\tau_0^d$  are set so that they are optimal for the Langmuir wave generation;<sup>35,36</sup> the driver amplitude  $a_0^d$  is set to be sufficiently high in order to excite a large amplitude nonlinear wave, which breaks in a controlled way and the driver duration  $\tau_0^d$  is chosen such that the wave is excited resonantly (i.e.,  $c\tau_0^d \approx \lambda_w/2$ ). The driver is linearly polarized with the electric field directed along the  $y$ -axis.

The wavelength of the source pulse is  $\lambda_0^s = 5 \lambda_0^d$ . By this choice, we keep  $\lambda_0^s$  sufficiently short so that the effects of plasma dispersion on the source are not significant but long enough to substantially reduce the computational demands of the simulations. The source has a semi-infinite flat-top temporal profile, which allows us to analyze the

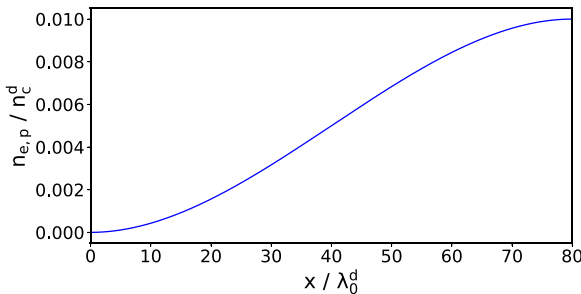


FIG. 1. Plot of the electron and proton density ramp profile used in the simulations.

simulation results more clearly. The normalized amplitude of the source,  $a_0^s$ , is varied in the simulations in order to thoroughly describe its impact on the reflection from the Langmuir wave. The source is linearly polarized in the direction perpendicular to the driver polarization (i.e., along the  $z$ -axis), and, thus, its electromagnetic field can be clearly distinguished.

Both laser pulses, the driver and the source, propagate in a pre-ionized uniform hydrogen plasma with electron and proton densities  $n_{e,p}^0 = 10^{-2} n_c^d$ , where  $n_c^d = m_e(\omega_0^d)^2/(4\pi e^2)$  is the critical plasma density with respect to the driver pulse. A smooth ramp is added to the left side of the target in order to reduce the effect of wave-breaking from a sharp rising plasma edge.<sup>40</sup> The ramp is defined by the function  $n_{e,p}(x) = n_{e,p}^0 (3 - 2(x - x_1)/(x_2 - x_1))((x - x_1)/(x_2 - x_1))^2$ , where  $x \in [x_1, x_2]$ . The values  $x_1 = 0$  and  $x_2 = 80 \lambda_0^d$  have proven to provide a sufficiently smooth transition [one can see the plot of the density ramp  $n_{e,p}(x)$  in Fig. 1]. The plasma is cold and collisionless. The electrons and protons are represented by quasi-particles with a triangular shape function. The number of quasi-particles per cell is 10 for both particle species. The smooth ramp in the plasma density profile is constructed by varying the weight of the quasi-particles (i.e., the number of real particles represented by each quasi-particle).

The simulations utilize a moving window technique,<sup>41</sup> which allows us to substantially decrease the length of the simulation domain. For this, the EPOCH code was modified in order to continuously introduce source pulse at the right boundary of the moving widow. The length of the simulation window is  $80 \lambda_0^d$ , and it moves along the

driver propagation direction at a velocity equal to  $c$ . The resolution of the Cartesian grid is 30 cells per theoretically estimated wavelength of the reflected radiation  $\lambda'$ . The value of  $\lambda'$  is calculated using Eq. (1), where we estimate  $\gamma_M \approx \omega_0^d/\omega_{pe}$ . The simulation domain thus contains  $1.92 \times 10^5$  cells in total, and the simulation time is set to  $450 T_0^d$ . The electromagnetic fields are calculated using the standard second-order Yee solver<sup>42</sup> with the CFL number<sup>43</sup> equal to 0.99. Absorbing boundary conditions are applied on each of the simulation domain sides for both the electromagnetic field and particles.

## B. Simulation results

First, we present the results of the simulation where the normalized amplitude of the source is relatively low,  $a_0^s = 10^{-4}$ , in order to avoid recoil effects and significant distortions of the Langmuir wave. The driver pulse starts to excite the Langmuir wave as soon as it enters the plasma. When the driver reaches the uniform plasma density region, the Langmuir wave takes the form of sharp electron density spikes separated by cavities. We consider the properties of the first electron density spike of the Langmuir wave formed behind the driver, which serves as a relativistic mirror. The first important parameter of the density spike in our study is its phase velocity because it determines the magnitudes of the carrier frequency upshift and electric field amplification of the reflected wave [see Eqs. (1) and (2)].

Figure 2(a) shows the evolution of the first electron density spike of the Langmuir wave behind the driver in the  $x - t$  plane, (b) its normalized phase velocity  $\beta_w$ , and (c) the corresponding relativistic Lorentz factor  $\gamma_w$ . The moment of wave-breaking,  $t \approx 190 T_0^d$ , in Fig. 2 is denoted by black dashed lines. It corresponds to the limit given by Eq. (12). At this moment, the electron density spike is centered around the point  $x \approx 150 \lambda_0^d$ . The reflectivity of the Langmuir wave becomes significant when the wave is closer to breaking.<sup>2</sup> After the wave-breaking, it is determined not only by the properties of the regular Langmuir wave but also by the properties of the injected electrons. From Fig. 2, it can be clearly seen that the Langmuir wave decelerates in uniform plasma, which is partially caused due to non-linear energy depletion of the driver<sup>45</sup> and due to the wave-breaking. The simulation results are analyzed from  $t_0 = 150 T_0^d$ , when the first density spike of the Langmuir wave can be clearly localized, until  $t_1 = 450 T_0^d$ . As can be seen from Fig. 2(c),  $\gamma_w \approx 1$  for  $t \geq t_1$ , and therefore, further reflection is not very interesting in the context of

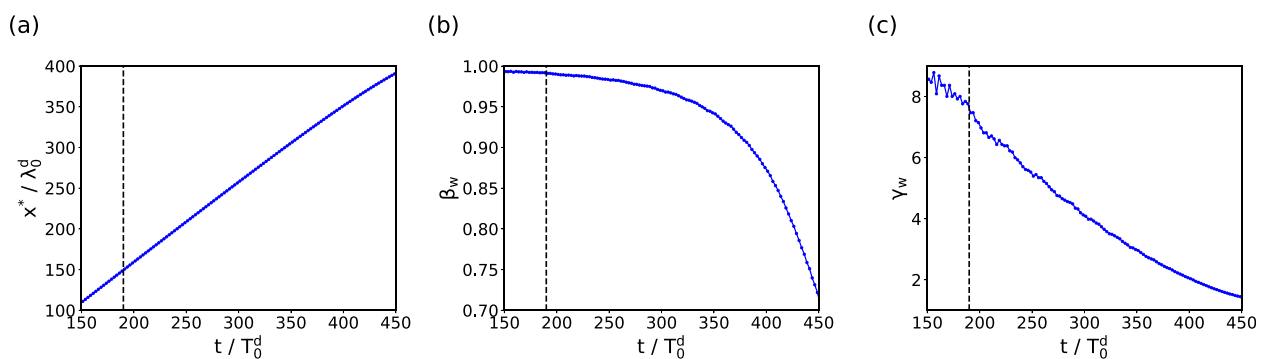
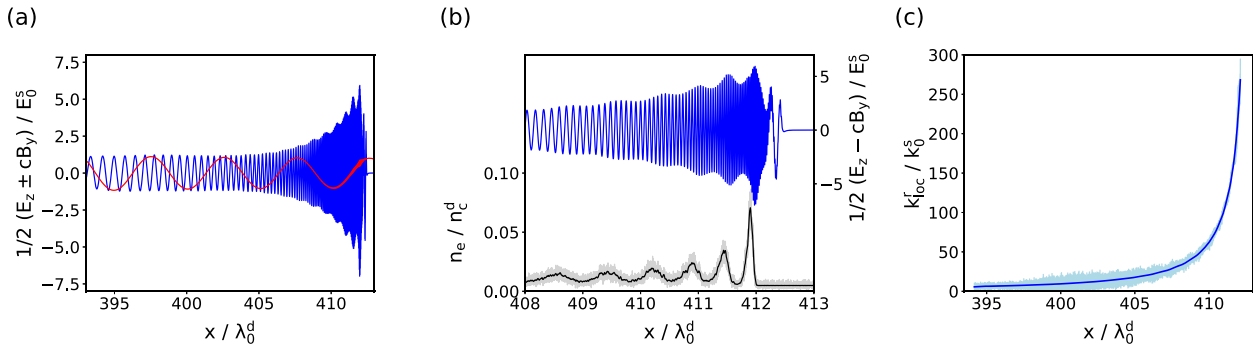


FIG. 2. The evolution of parameters of the first electron density spike of the Langmuir wave behind the driver in time. (a) The motion of the spike in the  $x - t$  plane, (b) the normalized phase velocity of the spike  $\beta_w$ , and (c) the corresponding relativistic Lorentz factor  $\gamma_w$ . The black dashed line marks the instant, when the Langmuir wave breaks.



**FIG. 3.** (a) Electromagnetic radiation incident at (red) and reflected from (blue) the first electron density spike of the Langmuir wave behind the driver, (b) details of the reflected electromagnetic wave (blue) with modulations correlated with the electron density (black), and (c) the evolution of the local carrier wavenumber of the reflected electromagnetic wave showing a negative chirp due to the Langmuir wave deceleration. The simulation data are observed at  $t = 450 T_0^d$ . In (b) and (c), the simulation data (light gray and light blue) are smoothed using the Savitzky–Golay filter<sup>44</sup> (black and blue).

the generation of coherent short-wavelength radiation [see Eq. (11)]. We also note that since the density spikes lag behind the fronts of light reflected from them, at  $t = t_1$ , the front of light reflected from the second density spike catches up with the first density spike,

$$c \int_{t_0}^{t_1} (1 - \beta_w(t)) dt \approx \lambda_w, \quad (18)$$

and thus, the radiation continuously reflected from the second density spike starts to interfere with the radiation reflected from the first density spike.

The spatial profile of the electromagnetic radiation reflected from the first density spike observed at  $t = 450 T_0^d$  is shown in Fig. 3(a). As can be clearly seen, its envelope is modulated. The modulations are caused by the electrons injected into the accelerating phase of the wake-field after the wave-breaking, which is shown in Fig. 3(b). Figure 3(c) displays the local carrier wavenumber of the reflected pulse. To obtain the local carrier wavenumber at any point in a reflected wavepacket, we first find the analytic signal from the original signal using the Hilbert transform.<sup>46</sup> The local carrier wavenumber is then obtained by differentiating the local phase (which corresponds to the phase angle of the analytic signal) with respect to  $x$ . It can be clearly seen that the reflected signal has a negative chirp, which corresponds to the mirror deceleration.

The wavelength of the reflected signal  $\lambda^r$  ranges from  $\approx 0.17 \lambda_0^s$  to  $\approx 3.3 \times 10^{-3} \lambda_0^s$ , and hence, the upshift factor with respect to  $\omega_0^s$  ranges from 6 to 298. Due to the effects of plasma dispersion, however, the wavelength of the source pulse interacting with the electron density spike is slightly larger than the vacuum wavelength,  $\lambda^s \approx 1.04 \lambda_0^s$ . Thus, the maximum factor of the frequency upshift with respect to  $\omega^s$  is about 310. From this frequency upshift factor using Eq. (11), we can estimate the relativistic Lorentz factor of the electron density spike as  $\gamma_w \approx 9.2$ , which corresponds to the instant of time  $t \approx 140 T_0^d$ .

Using the dependence of the local carrier wavenumber of the reflected pulse on the electron density spike coordinate  $k_{loc}^r(x)$  and the dependence of the spike coordinate on time  $x^*(t)$ , we obtain the time dependence of the frequency upshift factor of the reflected pulse,

$$\frac{\omega^r}{\omega_0^s} = \frac{k_0^s}{k_{loc}^r(x^*(t))}. \quad (19)$$

As seen in Fig. 4(a), the frequency upshift factor obtained in this way agrees very well with the calculation using Eq. (11) and the relativistic Lorentz factor of the electron density spike  $\gamma_w$  shown in Fig. 2(c).

Using the dependence of the reflected pulse electric field envelope amplitude on the spike coordinate  $E_{env}^r(x^*(t))$ , we obtain the time dependence of the electric field amplification factor

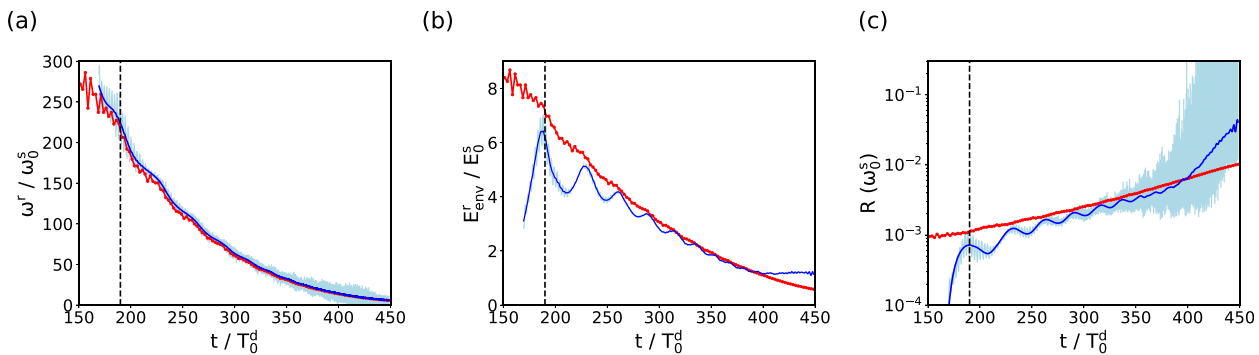


**FIG. 4.** The properties of the reflection from the first electron density spike of the Langmuir wave behind the driver. (a) The frequency upshift factor, (b) the electric field amplification factor, and (c) the instantaneous reflection coefficient in terms of the photon number. The simulation data (light blue) are smoothed using the Savitzky–Golay filter<sup>44</sup> (blue) and compared to analytical estimates (red). The black dashed line marks the instant, when the Langmuir wave breaks.

$$\frac{E_{env}^r}{E_0^s} = \frac{E_{env}^r(x^*(t))}{E_0^s}. \quad (20)$$

As seen in Fig. 4(b), the electric field amplification factor obtained in this way shows again fairly good conformity with the calculation using Eqs. (11) and (13) and the relativistic Lorentz factor of the electron density spike  $\gamma_w$  shown in Fig. 2(c). We find that the electric field amplification factor reaches its maximum at the moment of wave-breaking, with the electric field of the reflected pulse being amplified more than six times. Contrary to the analytical calculation, the amplification factor obtained from the simulation comprises visible oscillations. As discussed above, this feature corresponds to the modulations of the envelope of the reflected pulse caused by the electrons injected into the accelerating phase of the wakefield [see Fig. 3(b)].

Using the factors of the frequency upshift and the electric field amplification of the reflected pulse shown in Figs. 4(a) and 4(b), we reconstruct the instantaneous reflection coefficient of the electron

density spike in time, Fig. 4(c). For comparison, in Fig. 4(c), we also plot the instantaneous reflection coefficient computed using Eq. (13) and the relativistic Lorentz factor  $\gamma_w$  shown in Fig. 2(c). We find that the reflection coefficient in terms of the photon number grows from  $\approx 10^{-3}$  at the moment of wave-breaking up to  $\approx 5 \times 10^{-2}$  at the end of the interaction.

In order to investigate the recoil effects and explore the regimes around the threshold given by Eq. (16), we increase the amplitude of the source. Now, the source pulse encounters the electron density spike at the moment of wave-breaking ( $t = 190 T_0^d$ ). Its normalized amplitude  $a_0^s$  is varied from 0.01 to 1. The reflected radiation for the simulated cases can be seen in Fig. 5(a). In the case of  $a_0^s = 0.01$ , the interaction corresponds to the weak incident pulse approximation, and the impact of the source pulse is compensated by the electron flow that refreshes the structure of the density spike. For much larger amplitude,  $a_0^s = 1$ , only one cycle of the reflected wave is formed

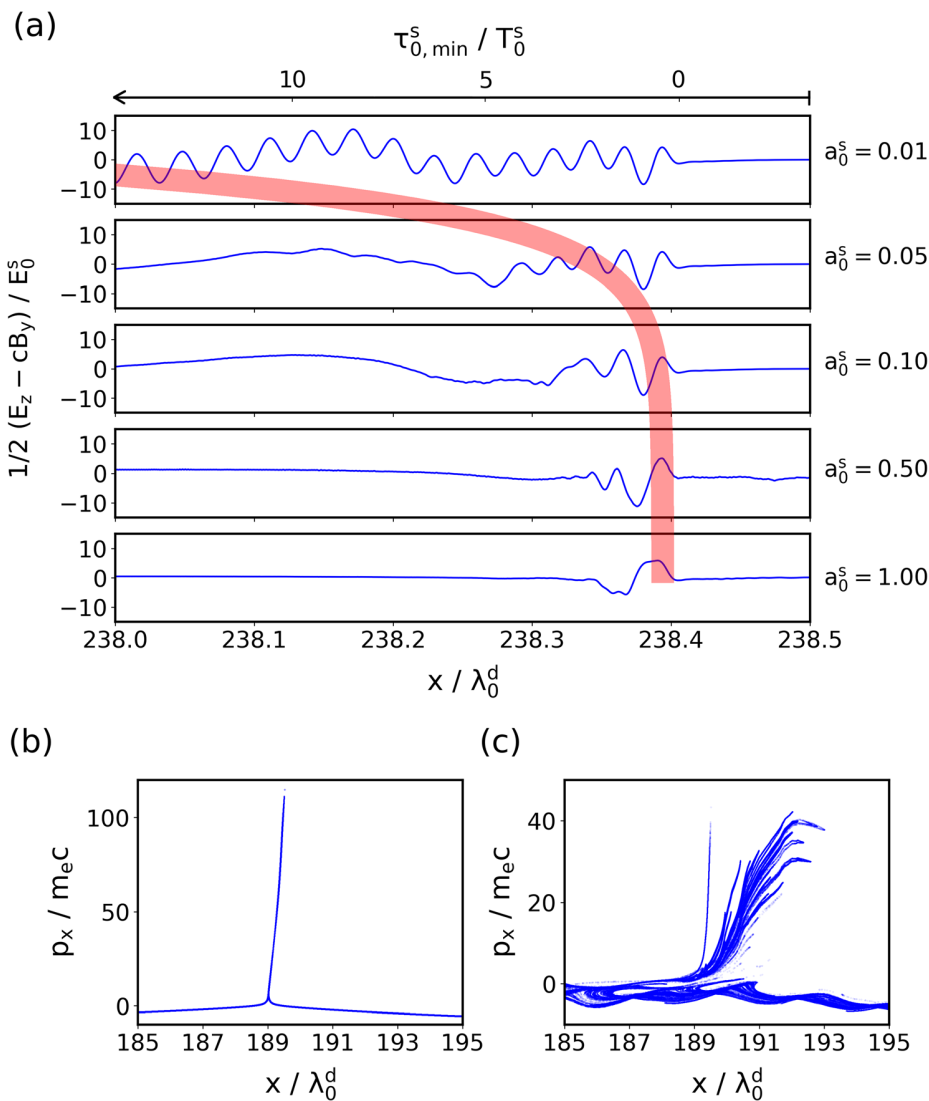


**FIG. 5.** Dependence of the reflected radiation on the amplitude of the source pulse. (a) Spatial profiles of the reflected wave for different source amplitudes. The thick red curve across the frames is the minimum source duration required for the recoil effect,  $\tau_{0,min}^s$ , according to Eq. (17) for  $\kappa = 1.5 \times 10^{-4}$ . The phase space of electrons at  $t = 230 T_0^d$  for (b)  $a_0^s = 0.01$  and (c)  $a_0^s = 1.0$ .

before the relativistic mirror is destroyed. Moreover, the radiation pressure of the source pulse in this case pushes the mirror back, which results in lower factors of the frequency upshift and the electric field amplification.

The threshold (17) gives the minimal duration of the incident electromagnetic wave necessary to cause a significant recoil on the relativistic mirror. In terms of normalized quantities, this duration can be rewritten as

$$\tau_{0,\min}^s = \frac{\varkappa}{4} \frac{n_e \lambda_w \lambda_0^s}{\gamma_w R(a_0^s)^2}, \quad (21)$$

where  $\tau_{0,\min}^s$  is normalized by  $T_0^s$ ,  $\lambda_0^s$ , and  $\lambda_w$  by  $\lambda_0^d$  and  $n_e$  by  $n_c^d$ . This quantity is shown in Fig. 5(a), for different source pulse amplitudes and  $\varkappa = 1.5 \times 10^{-4}$ . The value of the coefficient  $\varkappa$  is obtained from the comparison of the spatial profiles of the reflected wave for different incident wavepacket amplitudes. We assume that the duration  $\tau_{0,\min}^s$  roughly corresponds to the time period where the reflected wave coincides with the weak-source approximation. We see that for  $a_0^s = 0.01$ , the reflected wave corresponds to the weak-source approximation and classical double Doppler effect. Here,  $\tau_{0,\min}^s$  is very large. For  $a_0^s = 1$ , the recoil effects are well pronounced; the spatial profile of the reflected wave deviates from the weak-source approximation almost immediately. In this case,  $\tau_{0,\min}^s$  is almost zero. Between  $a_0^s = 0.01$  and  $a_0^s = 1$ , the properties of the spatial profile of the reflected wave correlate with the minimum source duration causing recoil effects given by Eq. (21), derived from the models (3)–(6).

A time span needed for a density spike to be fully refreshed by the electron flow can be roughly estimated as  $t_{ref} \approx \lambda_w/v_g^d \approx 20.53 T_0^d$ , where  $v_g^d$  is the group velocity of the driver pulse. During this time span, the density spike interacts approximately with 7.62 cycles of the source pulse. Therefore, if  $\tau_{0,\min}^s > 7.62 T_0^s$ , the impact of the source pulse on the density spike is compensated by the flow of electrons, and the interaction corresponds to the weak-source approximation. Using Eq. (21) with  $\varkappa = 1.5 \times 10^{-4}$ , this condition is equivalent to  $a_0^s < 0.026$ .

In Figs. 5(b) and 5(c), one can see the phase space of electrons located in the density spike illustrating the importance of the recoil effects of the relativistic mirror for two different amplitudes of the source pulse. For relatively small amplitudes, the structure of the electron density spike and the injected electrons (appearing after wave-breaking) are not affected, Fig. 5(b). When the intensity of the source pulse becomes sufficient to alter the motion of the electrons in the density spike, the spike splits into several layers, Fig. 5(c). The disappearance of the periodic structure of the reflected electromagnetic wave seen in Fig. 5(a) for  $a_0^s \geq 0.05$  is partially due to the destructive interference of waves reflected from the multi-layered structure of the split electron density spike and due to the recoil effects.

## V. CONCLUSION

We study the recoil effects of relativistic mirrors in the form of strongly nonlinear Langmuir waves driven by short intense laser pulses in underdense plasmas. This is important for the question of the feasibility of relativistic mirrors for the development of compact and tunable sources of coherent short-wavelength radiation. Using analytical calculations and PIC simulations, we investigate the properties of the Langmuir wave and the reflected pulse. We also find the threshold for the energy of the laser pulse incident on the electron

density spike above which the relativistic mirror undergoes significant recoil.

We show that the Langmuir wave driven by a short intense laser pulse in uniform plasma decelerates, and therefore, the reflected radiation has a negative chirp. We find that the electric field amplification factor of the reflected radiation reaches its maximum at the moment of wave-breaking. In addition, our results show that for a given intensity of the source pulse, there exists an optimal duration of the source pulse; longer-than-optimal pulses have a lower reflected-to-incident energy ratio. Moreover, for a given Langmuir wave excited by the driver pulse, there exists an optimal intensity of the source pulse, which provides the most intense reflected wave with almost the same frequency upshift factor as in the weak-source approximation.

The sources of coherent high-brightness radiation with wavelengths ranging from x-rays to gamma-rays are of great demand for many practical applications in diverse fields. Relativistic mirrors in laser plasmas can give a promising alternative for the development of radiation sources with tunable parameters at a significantly reduced size and cost in comparison with conventional devices.

## ACKNOWLEDGMENTS

This work was supported by the projects “High Field Initiative” (CZ.02.1.01/0.0/0.0/15\_003/0000449) from the European Regional Development Fund, “IT4Innovations National Supercomputing Center” (LM2015070) from The Ministry of Education, Youth and Sports of the Czech Republic, JSPS Kakenhi No. JP19H00669 and QST President’s Strategic Grant (Creative Research #20). The EPOCH code was in part funded by the UK EPSRC Grant Nos. EP/G054950/1, EP/G056803/1, EP/G055165/1, and EP/M022463/1.

## REFERENCES

- <sup>1</sup>A. Einstein, *Ann. Phys.* **322**, 891 (1905).
- <sup>2</sup>S. V. Bulanov, T. Z. Esirkepov, M. Kando, A. S. Pirozhkov, and N. N. Rosanov, *Phys.-Usp.* **56**, 429 (2013).
- <sup>3</sup>V. V. Kulagin, V. A. Cherepenin, M. S. Hur, and H. Suk, *Phys. Plasmas* **14**, 113101 (2007).
- <sup>4</sup>V. V. Kulagin, V. A. Cherepenin, M. S. Hur, and H. Suk, *Phys. Rev. Lett.* **99**, 124801 (2007).
- <sup>5</sup>T. Z. Esirkepov, S. V. Bulanov, M. Kando, A. S. Pirozhkov, and A. G. Zhidkov, *Phys. Rev. Lett.* **103**, 25002 (2009).
- <sup>6</sup>J. Meyer-Ter-Vehn and H. C. Wu, *Eur. Phys. J. D* **55**, 433 (2009).
- <sup>7</sup>S. S. Bulanov, A. Maksimchuk, K. Krushelnick, K. I. Popov, V. Y. Bychenkov, and W. Rozmus, *Phys. Lett., Sect. A* **374**, 476 (2010).
- <sup>8</sup>H. C. Wu, J. Meyer-Ter-Vehn, J. Fernández, and B. M. Hegelich, *Phys. Rev. Lett.* **104**, 234801 (2010).
- <sup>9</sup>H. C. Wu, J. Meyer-Ter-Vehn, B. M. Hegelich, and J. C. Fernández, *Phys. Rev. Spec. Top.—Accel. Beams* **14**, 170702 (2011).
- <sup>10</sup>H.-C. Wu and J. Meyer-ter Vehn, *Nat. Photonics* **6**, 304 (2012).
- <sup>11</sup>A. Andreev, K. Platonov, and S. Sadykova, *Appl. Sci.* **3**, 94 (2013).
- <sup>12</sup>D. Kiefer, M. Yeung, T. Dzelzainis, P. S. Foster, S. G. Rykovanov, C. L. Lewis, R. S. Marjoribanks, H. Ruhl, D. Habs, J. Schreiber, M. Zepf, and B. Dromey, *Nat. Commun.* **4**, 1763 (2013).
- <sup>13</sup>W. J. Ma, J. H. Bin, H. Y. Wang, M. Yeung, C. Kreuzer, M. Streeter, P. S. Foster, S. Cousens, D. Kiefer, B. Dromey, X. Q. Yan, J. Meyer-Ter-Vehn, M. Zepf, and J. Schreiber, *Phys. Rev. Lett.* **113**, 235002 (2014).
- <sup>14</sup>S. V. Bulanov, N. M. Naumova, and F. Pegoraro, *Phys. Plasmas* **1**, 745 (1994).
- <sup>15</sup>R. Lichters, J. Meyer-ter Vehn, and A. Pukhov, *Phys. Plasmas* **3**, 3425 (1996).

- <sup>16</sup>N. M. Naumova, J. A. Nees, I. V. Sokolov, B. Hou, and G. A. Mourou, *Phys. Rev. Lett.* **92**, 63902 (2004).
- <sup>17</sup>T. Baeva, S. Gordienko, and A. Pukhov, *Phys. Rev. E* **74**, 46404 (2006).
- <sup>18</sup>J. Wheeler, A. Borot, A. Malvache, A. Ricci, A. Jullien, R. Lopez-Martens, S. Monchocé, H. Vincenti, and F. Quéré, *Nat. Photonics* **6**, 829 (2012).
- <sup>19</sup>H. Vincenti, *Phys. Rev. Lett.* **123**, 105001 (2019).
- <sup>20</sup>A. S. Pirozhkov, S. V. Bulanov, T. Z. Esirkepov, M. Mori, A. Sagisaka, and H. Daido, *Phys. Plasmas* **13**(1), 013107 (2006).
- <sup>21</sup>A. S. Pirozhkov, S. V. Bulanov, T. Z. Esirkepov, A. Sagisaka, T. Tajima, and H. Daido, “Intensity scalings of attosecond pulse generation by the relativistic-irradiance laser pulses,” in *Ultrafast Optics*, Springer Series in Optical Sciences Vol. 132, edited by S. Watanabe and K. Midorikawa (Springer, New York, 2007), pp. 265–272.
- <sup>22</sup>S. V. Bulanov, T. Esirkepov, and T. Tajima, *Phys. Rev. Lett.* **91**, 85001 (2003).
- <sup>23</sup>M. Kando, Y. Fukuda, A. S. Pirozhkov, J. Ma, I. Daito, L. M. Chen, T. Z. Esirkepov, K. Ogura, T. Homma, Y. Hayashi, H. Kotaki, A. Sagisaka, M. Mori, J. K. Koga, H. Daido, S. V. Bulanov, T. Kimura, Y. Kato, and T. Tajima, *Phys. Rev. Lett.* **99**, 135001 (2007).
- <sup>24</sup>A. S. Pirozhkov, J. Ma, M. Kando, T. Z. Esirkepov, Y. Fukuda, L. M. Chen, I. Daito, K. Ogura, T. Homma, Y. Hayashi, H. Kotaki, A. Sagisaka, M. Mori, J. K. Koga, T. Kawachi, H. Daido, S. V. Bulanov, T. Kimura, Y. Kato, and T. Tajima, *Phys. Plasmas* **14**, 123106 (2007).
- <sup>25</sup>M. Kando, A. S. Pirozhkov, K. Kawase, T. Z. Esirkepov, Y. Fukuda, H. Kiriyama, H. Okada, I. Daito, T. Kameshima, Y. Hayashi, H. Kotaki, M. Mori, J. K. Koga, H. Daido, A. Y. Faenov, T. Pikuz, J. Ma, L. M. Chen, E. N. Ragozin, T. Kawachi, Y. Kato, T. Tajima, and S. V. Bulanov, *Phys. Rev. Lett.* **103**, 235003 (2009).
- <sup>26</sup>M. Lobet, M. Kando, J. K. Koga, T. Z. Esirkepov, T. Nakamura, A. S. Pirozhkov, and S. V. Bulanov, *Phys. Lett., Sect. A* **377**, 1114 (2013).
- <sup>27</sup>J. K. Koga, S. V. Bulanov, T. Z. Esirkepov, M. Kando, S. S. Bulanov, and A. S. Pirozhkov, *Plasma Phys. Controlled Fusion* **60**, 074007 (2018).
- <sup>28</sup>H. Moghadasin, A. R. Niknam, D. Komaizi, and M. Banjafar, *Phys. Plasmas* **26**, 093105 (2019).
- <sup>29</sup>J. Mu, T. Z. Esirkepov, P. Valenta, T. M. Jeong, Y. Gu, J. K. Koga, A. S. Pirozhkov, M. Kando, G. Korn, and S. V. Bulanov, *Phys. Wave Phenom.* **27**, 247 (2019).
- <sup>30</sup>J. K. Koga, S. V. Bulanov, T. Z. Esirkepov, A. S. Pirozhkov, M. Kando, and N. N. Rosanov, *Phys. Rev. A* **86**, 53823 (2012).
- <sup>31</sup>P. Chen and G. Mourou, *Phys. Rev. Lett.* **118**, 45001 (2017).
- <sup>32</sup>S. V. Bulanov, T. Esirkepov, V. S. Khoroshkov, A. V. Kuznetsov, and F. Pegoraro, *Phys. Lett., Sect. A* **299**, 240 (2002).
- <sup>33</sup>R. Neutze, R. Wouts, D. Van Der Spoel, E. Weckert, and J. Hajdu, *Nature* **406**, 752 (2000).
- <sup>34</sup>F. Krausz and M. Ivanov, *Rev. Mod. Phys.* **81**, 163 (2009).
- <sup>35</sup>S. V. Bulanov, T. Z. Esirkepov, Y. Hayashi, H. Kiriyama, J. K. Koga, H. Kotaki, M. Mori, and M. Kando, *J. Plasma Phys.* **82**, 905820308 (2016).
- <sup>36</sup>E. Esarey, C. B. Schroeder, and W. P. Leemans, *Rev. Mod. Phys.* **81**, 1229 (2009).
- <sup>37</sup>A. Akhiezer and R. Polovin, Sov. Phys. JETP **3**, 696 (1956).
- <sup>38</sup>*Handbook of Mathematical Functions*, edited by M. Abramowitz and I. A. Stegun, Applied Mathematical Series, Vol. 55 (National Bureau of Standards, Washington, 1964).
- <sup>39</sup>T. D. Arber, K. Bennett, C. S. Brady, A. Lawrence-Douglas, M. G. Ramsay, N. J. Sircombe, P. Gillies, R. G. Evans, H. Schmitz, A. R. Bell, and C. P. Ridgers, *Plasma Phys. Controlled Fusion* **57**, 113001 (2015).
- <sup>40</sup>S. V. Bulanov, I. N. Inovenkov, N. M. Naumova, and A. S. Sakharov, Sov. J. Plasma Phys. **16**, 444 (1990).
- <sup>41</sup>B. Fidel, E. Heyman, R. Kastner, and R. W. Ziolkowski, *J. Comput. Phys.* **138**, 480 (1997).
- <sup>42</sup>K. S. Yee, *IEEE Trans. Antennas Propag.* **14**, 302 (1966).
- <sup>43</sup>R. Courant, K. Friedrichs, and H. Lewy, *Math. Ann.* **100**, 32 (1928).
- <sup>44</sup>A. Savitzky and M. J. Golay, *Anal. Chem.* **36**, 1627 (1964).
- <sup>45</sup>S. V. Bulanov, I. N. Inovenkov, V. I. Kirsanov, N. M. Naumova, and A. S. Sakharov, *Phys. Fluids B* **4**, 1935 (1992).
- <sup>46</sup>F. W. King, *Hilbert Transforms*, Encyclopedia of Mathematics and its Applications Vol. 2 (Cambridge University Press, 2009).



#### A.4 Relativistic flying forcibly oscillating reflective diffraction grating

## Relativistic flying forcibly oscillating reflective diffraction grating

Jie Mu,<sup>1</sup> Timur Zh. Esirkepov<sup>1,2,\*</sup> Petr Valenta<sup>1,3</sup> Yanjun Gu,<sup>1</sup> Tae Moon Jeong<sup>1,4</sup> Alexander S. Pirozhkov<sup>1,5</sup>  
James K. Koga<sup>1,6</sup> Masaki Kando<sup>1,2</sup> Georg Korn,<sup>1</sup> and Sergei V. Bulanov<sup>1,2</sup>

<sup>1</sup>ELI Beamlines Project, Institute of Physics of the ASCR, Na Slovance 2, 18221 Prague, Czech Republic

<sup>2</sup>Kansai Photon Science Institute, National Institutes for Quantum and Radiological Science and Technology, 8-1-7 Umemidai, Kizugawa, Kyoto 619-0215, Japan

<sup>3</sup>Faculty of Nuclear Sciences and Physical Engineering, Czech Technical University in Prague, Brehova 7, 11519 Prague, Czech Republic



(Received 30 June 2020; accepted 8 October 2020; published 2 November 2020)

Relativistic flying forcibly oscillating reflective diffraction gratings are formed by an intense laser pulse (driver) in plasma. The mirror surface is an electron density singularity near the joining area of the wake wave cavity and the bow wave; it moves together with the driver laser pulse and undergoes forced oscillations induced by the field. A counterpropagating weak laser pulse (source) is incident at grazing angles, being efficiently reflected and enriched by harmonics. The reflected spectrum consists of the source pulse base frequency and its harmonics, multiplied by a large factor due to the double Doppler effect.

DOI: [10.1103/PhysRevE.102.053202](https://doi.org/10.1103/PhysRevE.102.053202)

### I. INTRODUCTION

Bright sources of electromagnetic radiation with the spectral range from extreme ultraviolet to x rays have attracted a great deal of attention because of their great potential for both fundamental science and practical applications (e.g., in biology, medicine, and materials science) [1,2]. One of the ways toward developing ultrashort intense electromagnetic pulse sources is a simultaneous frequency upshift and pulse compression. This occurs in the reflection of an electromagnetic wave from a fast approaching mirror, which is a manifestation of the double Doppler effect. According to the Einstein prediction [3], in the head-on wave-mirror collision, the reflected electromagnetic pulse is compressed and its frequency is upshifted by the same factor  $(c + v_M)/(c - v_M) \approx 4\gamma_M^2$ , where  $v_M$  is the mirror velocity,  $c$  is the speed of light in vacuum, and  $\gamma_M = (1 - v_M^2/c^2)^{-1/2}$  is the mirror Lorentz factor.

There are a few physical realizations of this concept. Perhaps the earliest are the electromagnetic wave reflection at a moving relativistic electron slab [4] and at moving ionization fronts [5–7].

A potentially high repetition generation of frequency-upshifted high-intensity quasimonochromatic electromagnetic pulses [8–11] uses a laser-driven breaking wake wave in underdense plasma as the relativistic flying mirrors (RFMs) which reflect, compress, and focus a counterpropagating laser pulse (for details see the reviews in [12,13] and references therein). An increase of the intensity of counterpropagating laser pulses modifies this scheme, adding generation of high-order harmonics at the mirror [14]; the spectrum of the reflected light consists of harmonics of the incident pulse base frequency, all multiplied by approximately  $4\gamma_M^2$ .

The flying mirror can be a laser-accelerated thin electron layer ejected by an intense laser pulse from a thin foil [15]. An ensemble of flying mirrors producing high-intensity attosecond pulses is realized by electron layers consequently ejected at every period of the intense incident laser [16]. Due to multiple reflections on many semitransparent electron layers, the conversion efficiency can be as high as  $4\gamma_M^2 \gg 1$ , where energy is gained via the momentum transfer from the flying electron layers to the reflected radiation [16].

The relativistic oscillating mirrors (ROMs) are formed at the surface of an overdense plasma, when a strong laser field both induces the nonlinearly oscillating electron density modulations and gets reflected off them, producing high-order harmonics [17–19]. When a dense plasma slab is accelerated by a high-contrast ultraintense laser pulse in the regime of radiation pressure dominant acceleration, it gains energy as a receding mirror and acts as an approaching mirror for a counterpropagating intense laser pulse [20]; in addition, it acts as a relativistic oscillating mirror in the comoving reference frame so that the reflected radiation contains high-order harmonics, upshifted due to the double Doppler effect.

Here we present a physical realization of the relativistic mirror, the relativistic flying forcibly oscillating mirror (RFFOM). It appears as a surface of high electron density corresponding to a folding singularity created by an intense laser pulse propagating in plasma. Being modulated by the laser field, this surface acts as a reflective diffraction grating for a counterpropagating electromagnetic wave.

The paper is organized as follows. In Sec. II the mechanism of the RFFOM concept is introduced. Section III gives a simplified theory based on the assumption of an inclined ideal flat mirror. Section IV introduces the simulation setup and the basic parameters. In Secs. V and VI we analyze the properties of the reflected wave and its spectrum using a three-dimensional (3D) simulation and high-resolution 2D simulations, respectively. In Sec. VII the influence of thermal

\*timur.esirkepov@qst.go.jp

effects on the RFFOM is investigated. Section VIII summarizes the results and discusses possible applications of the concept.

## II. RFFOM MECHANISM

An intense laser pulse propagating in underdense plasma excites wake waves [21–23]. The laser field pushes electrons not only along the laser axis, but also aside, creating a cavity void of electrons. Depending on the relation between the kinetic energy of transversely pushed electrons  $\mathcal{E}_{e\perp}$  and the electrostatic potential of the cavity  $\varphi$ , one can see three patterns of the first wake wave period. When  $\mathcal{E}_{e\perp} \ll e\varphi$ , the cavity rear has a smooth surface, which can be used as a RFM [8]. Here  $e$  is the electron charge. For  $\mathcal{E}_{e\perp} \gtrsim e\varphi$ , electrons forming the cavity wall overshoot the axis at the cavity rear, which causes the transverse wake wave breaking [24], playing an important role in the electron injection into the acceleration phase of the wake wave. A tightly focused laser pulse can push electrons so that  $\mathcal{E}_{e\perp} \gg e\varphi$  and electrons form a bow wave [25], which detaches from the cavity wall in the head of the laser pulse. A propagation of transversely pushed electrons through unperturbed electrons is a multistream flow. In the approximation of a continuous electron fluid, such flows have density singularities whose existence, universality, and structural stability are explained by catastrophe theory [26]. The fold singularity corresponds to the electron density jumps at the cavity wall and bow wave boundary. At their joining, the electron density is even higher and corresponds to the cusp singularity. The fold singularity is indeed a fold of the phase distribution of initially unperturbed electrons, projected into a space to form the density distribution [27–29].

The cusp and the adjacent folds act as a pair of mirrors joined at some angle (cusped mirror), which undergoes forced oscillations induced by the laser field (Fig. 1). It partially reflects a counterpropagating electromagnetic wave (source). The reflected radiation is enriched by high-order harmonics, because the cusped mirror is oscillating, like ROMs [17], and all of the reflected spectrum is upshifted because the cusped mirror moves with a high speed, like RFMs [8]. Moreover, the source can have a grazing incidence on the mirror surfaces, because at the point of the bow wave detachment from the cavity wall, the surfaces of the highest electron density can make a relatively small angle with respect to the laser axis. These angles can be controlled by the laser focal spot size and initial plasma density, in accordance with the condition of the bow wave formation [25]. As is known, the smaller the grazing incidence angle, the higher the reflection efficiency. In our case, however, the increase of the reflection efficiency is accompanied by a decrease of the frequency upshift factors.

The cusped mirror is a RFFOM, combining the properties of a RFM and a ROM. The surface of the cusped mirror is periodically modulated by the laser field; therefore, the cusped mirror has the properties of a reflective diffraction grating.

A source laser pulse is reflected from the cusped mirror; high-order harmonics are generated due to the mirror oscillations as in ROMs and the whole reflected spectrum is upshifted as in RFMs. The reflected radiation goes at discrete angles corresponding to the diffraction orders of a relativistic flying reflective diffraction grating. The feasibility of the

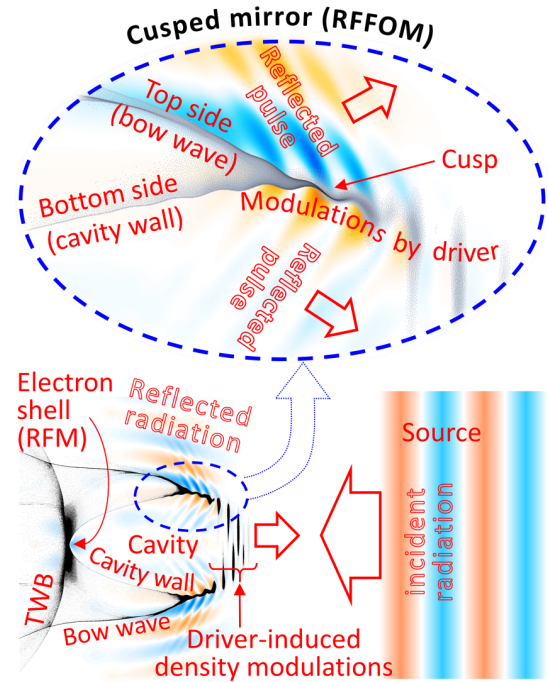


FIG. 1. The RFFOM scheme. On the bottom the driver pulse (not shown but revealed via density modulations) creates a cavity and bow wave in underdense plasma (2D PIC simulation of Sec. VI). Over-shooting electrons cause transverse wave breaking (TWB). Shown on top is a close-up of the area near the cusp. A counterpropagating source pulse is reflected off the sides of the cusped mirror, forcibly oscillating under the action of the driver. The blue-red color scale is for the electric field and grayscale is for the electron density.

above-described RFFOM is demonstrated using 2D and 3D particle-in-cell (PIC) simulations.

We note that the cusp and the portions of adjacent folds have their own self-emission [27–30] when only the driver pulse is present. In particular, the cusp emits high-frequency electromagnetic radiation in a cone around the vector of the average velocity of the cusp. The constructive interference is gained only for wavelengths which are emitted by the regions having size shorter than the wavelength in the radiation propagation direction. This condition is always satisfied for the cusp singularity. In analogy with the moving oscillating charge, the cusp emits the high-order harmonics observed in experiments [27–29]. Here we do not consider this self-emission. In the simulations shown below, the source pulse and consequently the reflected pulse have different polarization with respect to the driver and the reflected radiation disappears in the absence of the source.

## III. MODEL

In order to analyze the base frequency and direction angle of electromagnetic radiation reflected from the cusped mirror, we use a simplified model, neglecting oscillations of the mirror surface (Fig. 2). We consider a moving ideal flat mirror in a 2D space ( $x, y$ ), where the mirror velocity vector is  $\{\beta c, 0\}$ , with  $\beta = v_M/c$ . The mirror is inclined with respect to its velocity; the normal vector to its surface

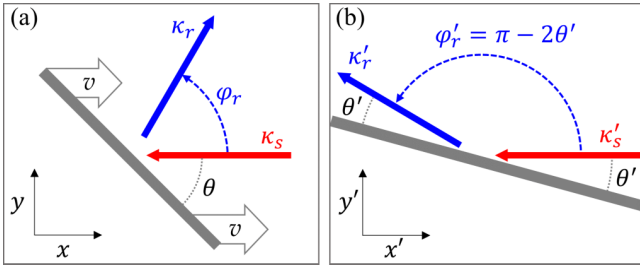


FIG. 2. Positional relationship of the moving inclined mirror, and incident and reflected waves in the (a) laboratory and (b) comoving reference frames.

is  $\{\sin \theta, \cos \theta\}$ . A counterpropagating electromagnetic wave with frequency  $\omega_s$  is incident on the mirror; its wave number vector is  $\kappa_s = \{-\omega_s/c, 0\}$ . The reflected electromagnetic wave has a frequency of  $\omega_r$  and a wave number vector of  $\kappa_r = (\omega_r/c)\{\cos \phi_r, \sin \phi_r\}$ .

The parameters of the reflected wave are obtained by changing to the reference frame of the mirror, considering specular reflection, and changing back to the laboratory reference frame

$$\omega_r = \omega_s \frac{1 + \beta}{1 - \beta \cos \phi_r}, \quad (1)$$

$$\cos \phi_r = \frac{(1 + \beta)^2 \tan^2(\theta) - 1}{(1 + \beta)^2 \tan^2(\theta) + 1}. \quad (2)$$

For large values of  $\gamma = (1 - \beta^2)^{-1/2} \rightarrow \infty$  and fixed angle  $0 \leq \theta \leq \pi/2$ , we have

$$\omega_r = \omega_s \frac{5 - 3 \cos 2\theta}{1 + \cos 2\theta} - O\left(\frac{1}{\gamma^2}\right), \quad (3)$$

$$\cos \phi_r = \frac{3 - 5 \cos 2\theta}{5 - 3 \cos 2\theta} + O\left(\frac{1}{\gamma^2}\right). \quad (4)$$

We note that the expansion of Eq. (3) diverges for  $\theta \rightarrow \pi/2$  (i.e., for near-normal incidence). Nevertheless, the larger the  $\gamma$ , the greater the well-approximated threshold for  $\theta$ ; for example, for  $\gamma = 10$ , the approximation is good for  $0 \leq \theta \leq \pi/4$  with the maximum (overestimation) error of 2%. In Eq. (4) the expansion is valid for the whole interval of  $0 \leq \theta \leq \pi/2$ ; for example, for  $\gamma = 10$ , the maximum (overestimation) error is 0.25%. In the limit of the glancing angle  $\theta \rightarrow 0$ , reflection does not occur:  $\omega_r \rightarrow \omega_s$  and  $\cos \phi_r = -1$ .

According to Eqs. (3) and (4), for large  $\gamma$ , the mirror inclined at  $\theta = \arccos(\frac{3}{5})/2 \approx 26.6^\circ$  reflects radiation at  $90^\circ$  with frequency  $\omega_r \approx 2\omega_s$ . If the driver pulse is sufficiently intense and tightly focused (e.g., due to relativistic self-focusing), the transversely pushed electrons move with relativistic velocity. Since the driver velocity is also relativistic, the bow wave outer boundary makes an angle of  $\theta \approx 45^\circ$  with the laser axis [25]. In this case, from the expansions in Eqs. (3) and (4) we obtain  $\omega_r \approx 5\omega_s$  and  $\phi_r \approx \arccos(\frac{3}{5}) \approx 53^\circ$ , independent of the mirror velocity for sufficiently large  $\gamma$ .

Equation (1) represents an ellipse in polar coordinates  $(\omega_s, \phi_r)$  [9]. In the coordinates  $(k_x, k_y)$ , which are the components of the reflected wave number vector  $\kappa_r = \{k_x, k_y\}$ , we have  $\omega_r = c(k_x^2 + k_y^2)^{1/2}$  and  $\phi_r = \arctan(k_y/k_x)$ , so the

leftmost focus of the ellipse is at  $(0,0)$  and the major axis coincides with the  $x$  axis; the leftmost point of the ellipse is  $\omega_r|_{\phi_r=\pi} = \omega_s$ , which means transmitted radiation; the rightmost point of the ellipse is  $\omega_r|_{\phi_r=0} = \omega_s(1 + \beta)/(1 - \beta) \approx 4\gamma^2\omega_s$ , which means exactly backward reflection. If there exist harmonics of the base frequency, each harmonic order sits on its own ellipse with the same leftmost focus.

If the source pulse has sufficiently low frequency, its wavelength inside the plasma is significantly longer than in vacuum,  $\tilde{\lambda}_s = \lambda_s(1 - \omega_{pe}^2/\omega_s^2)^{-1/2}$ , where  $\omega_{pe} = \sqrt{4\pi e^2 n_e/m_e}$  is the Langmuir frequency. Here  $n_e$  is the electron density and  $m_e$  is the electron mass. In this situation, Eq. (1) becomes [12]

$$\omega_r = \frac{\psi_s + \beta \cos(\phi_r) \sqrt{\psi_s^2 - \omega_{pe}^2(1 - \beta^2 \cos^2 \phi_r)}}{1 - \beta^2 \cos^2 \phi_r}, \quad (5)$$

$$\psi_s = \omega_s + \beta \sqrt{\omega_s^2 - \omega_{pe}^2} \quad (6)$$

and the reflection angle is determined by the relation

$$\frac{\sin \phi_r}{\cos(\phi_r) - \beta \beta_{s,ph}} = \frac{2\gamma^2 \tan \theta}{\tan^2(\theta) - \gamma^2}, \quad (7)$$

where  $\beta_{s,ph} = v_{s,ph}/c > 1$  is the normalized phase velocity of the source pulse,

$$\begin{aligned} \beta_{s,ph} &= \omega_r / \sqrt{\omega_r^2 - \omega_{pe}^2} \\ &= \frac{\psi_s + \beta \cos(\phi_r) \sqrt{\psi_s^2 - \omega_{pe}^2(1 - \beta^2 \cos^2 \phi_r)}}{\psi_s \beta \cos(\phi_r) + \sqrt{\psi_s^2 - \omega_{pe}^2(1 - \beta^2 \cos^2 \phi_r)}}. \end{aligned} \quad (8)$$

In the limit  $\omega_{pe} \rightarrow 0$  and  $\psi_s \rightarrow (1 + \beta)\omega_s$ , Eq. (5) reduces to Eq. (1). According to Eq. (5), the maximum frequency upshift (at  $\phi_r = 0$ ) in plasma is slightly less than that in vacuum,

$$\begin{aligned} \omega_r|_{\phi_r=0} &= \gamma^2 (\psi_s + \beta \sqrt{\psi_s^2 - \omega_{pe}^2/\gamma^2}) \\ &< \gamma^2 (1 + \beta) \psi_s. \end{aligned} \quad (9)$$

#### IV. SIMULATION SETUP

To study the laser plasma interaction under the conditions when the bow wave is formed, we carry out 2D and 3D PIC simulations using the EPOCH code [31] and REMP code [32]. The plasma is fully ionized and homogeneous. The ion response is neglected due to a large ion-to-electron mass ratio, relatively low electron density, and a short time of the considered interaction. The electron density is  $n_e = 1.14 \times 10^{19} \text{ cm}^{-3} \times (1 \text{ } \mu\text{m}/\lambda_d)^2 = 0.01 n_c$ , where  $n_c = \pi/r_e \lambda_d^2 = 1.115 \times 10^{21} \text{ cm}^{-3} \times (1 \text{ } \mu\text{m}/\lambda_d)^2$  is the critical density,  $r_e = e^2/m_e c^2$  is the classical electron radius, and  $\lambda_d = 2\pi c/\omega_d$  is the wavelength, with  $\omega_d$  the frequency of the driver laser and  $c$  the speed of light in vacuum.

The driver laser pulse is linearly polarized with its electric field vector along the  $y$  axis and its dimensionless amplitude is  $a_d = eE_d/m_e \omega_d c = 6.62$ , corresponding to an intensity of  $I_d = 6 \times 10^{19} \times (1 \text{ } \mu\text{m}/\lambda_d)^2 \text{ W/cm}^2$ , where  $E_d$  is the maximum electric field of the driver. Its full width at half maximum is  $5\lambda_d \times 5\lambda_d$  (along the  $x$  and  $y$  axes) in 2D simulations and  $10\lambda_d \times 4\lambda_d \times 4\lambda_d$  (along the  $x$ ,  $y$ , and  $z$  axes) in the 3D

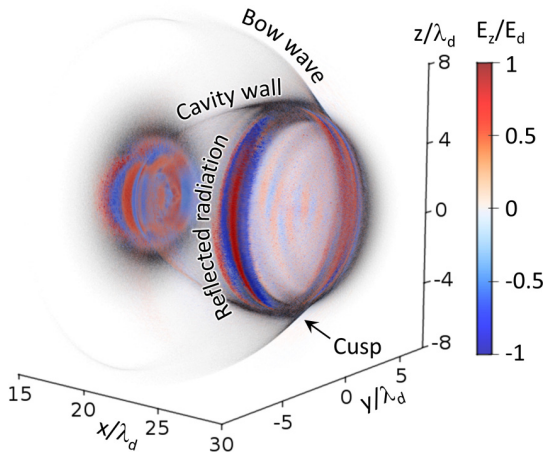


FIG. 3. Wake wave cavity, bow wave, and cusp seen in the electron density distribution (in grayscale). The reflected electric field normalized to that of the driver  $E_d$  is shown by the blue-red color scale.

simulation. The driver focus is at the left boundary of the simulation box. In the 3D simulation, the transverse sizes of the driver and source laser pulses are less than in 2D simulations due to the limited computational resources.

The source laser pulse has perpendicular polarization; its electric field vector is along the  $z$  axis. This helps to distinguish the driver, the source, and the reflected radiation, as was done in previous publications [8]. Moreover, it helps to distinguish the reflected signal from the cusp self-emission. The source has a longer wavelength  $\lambda_s = 8\lambda_d$ . This helps to more easily resolve and analyze the strongly upshifted reflected radiation enriched with high-order harmonics with limited computing resources. The source pulse dimensionless amplitude is  $a_s = 0.05$ , corresponding to an intensity of  $I_s = 5.35 \times 10^{13} \text{ W/cm}^2$ . It is sufficiently weak in order not to affect the motion and structure of the cusped mirror [33]. Its full width at half maximum is  $8\lambda_d \times 20\lambda_d$  in 2D simulations and  $8\lambda_d \times 10\lambda_d \times 10\lambda_d$  in the 3D simulation. Its transverse size is large enough to see reflection from bow waves.

The simulation results are shown in Figs. 7(a), where Figs. 3 and 4 represent 3D simulation while Figs. 5–9 show 2D simulations with similar parameters. In the following  $T_d = \lambda_d/c$  is the period of the driver laser cycle.

### V. 3D SIMULATION

An excitation of the wake wave and bow wave by the driver pulse, the formation of the cavity, and the reflection of the source pulse from the cusped mirror can be seen in the 3D PIC simulation (Fig. 3). Here the simulation box has a size of  $30\lambda_d \times 30\lambda_d \times 30\lambda_d$ . The spatial grid mesh is  $\Delta x/\lambda_d = \frac{1}{30}$ ,  $\Delta y/\lambda_d = \frac{1}{30}$ , and  $\Delta z/\lambda_d = \frac{1}{30}$ . Plasma uniformly fills the cube with coordinates of  $0\lambda_d \leq x \leq 30\lambda_d$ ,  $-15\lambda_d \leq y \leq 15\lambda_d$ , and  $-15\lambda_d \leq z \leq 15\lambda_d$ . The total number of quasiparticles is  $5.7 \times 10^8$ .

The reflected radiation in Fig. 3 is computed as follows. First, the difference is taken between the electromagnetic fields in two separate simulations, one with the source pulse and another without it. The electromagnetic field obtained in

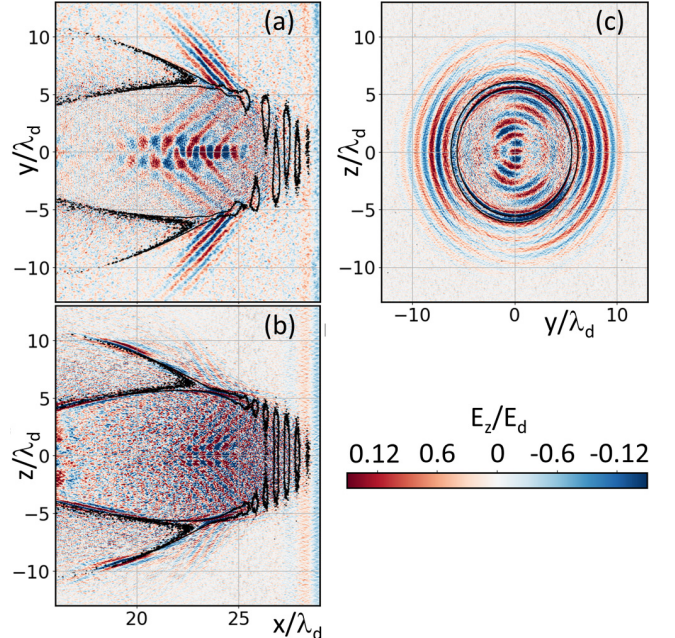


FIG. 4. Cross sections of the box shown in Fig. 3 along the planes (a)  $(x, y, z = 0)$ , (b)  $(x, y = 0, z)$ , and (c)  $(x = 22.5, y, z)$ . The blue-red color scale for the electric field normalized to that of the driver  $E_d$  contours for electron density.

this way represents the incident source pulse together with the reflected radiation [10]. Second, the low-frequency component is filtered out, thus the field representing the source pulse is removed so that the remaining component corresponds to the reflected radiation.

As can be seen in Figs. 3 and 4(a), reflection occurs in the regions of high electron density. Reflection starts at the cusp, a location where the cavity wall joins the outline of the bow wave. Then it happens at the rear of the cavity. The latter is a realization of the RFM by the breaking wake wave, as described in Ref. [8].

Here we focus on the reflection at the cusp. As can be seen in Figs. 4(a) and 4(c), the reflected radiation goes at some angle off axis, from both sides of the cusped mirror near the cusp, in the form of two short-wavelength pulses: An outer pulse initially goes outside the cavity and an inner pulse initially goes inside the cavity. As expected, the reflected radiation wavefronts correspond to a conical mirror; in particular, the cross section in the plane of the driver axis and polarization demonstrates a nearly flat wave front cross section [Fig. 4(a)], in agreement with the model assumption in Sec. III. These fronts certainly become almost spherical when the reflected pulses propagate at a distance much greater than their width.

The frequency upshift of the reflected radiation is obvious: The reflected pulse wavelength is significantly shorter than the electron density modulation induced by the driver, which in turn is much shorter than the source pulse wavelength ( $\omega_s = \omega_d/8$ ). We note that the outer pulse has a shorter wavelength than the inner pulse, in accordance with their propagation direction, which corresponds to reflection from different sides of

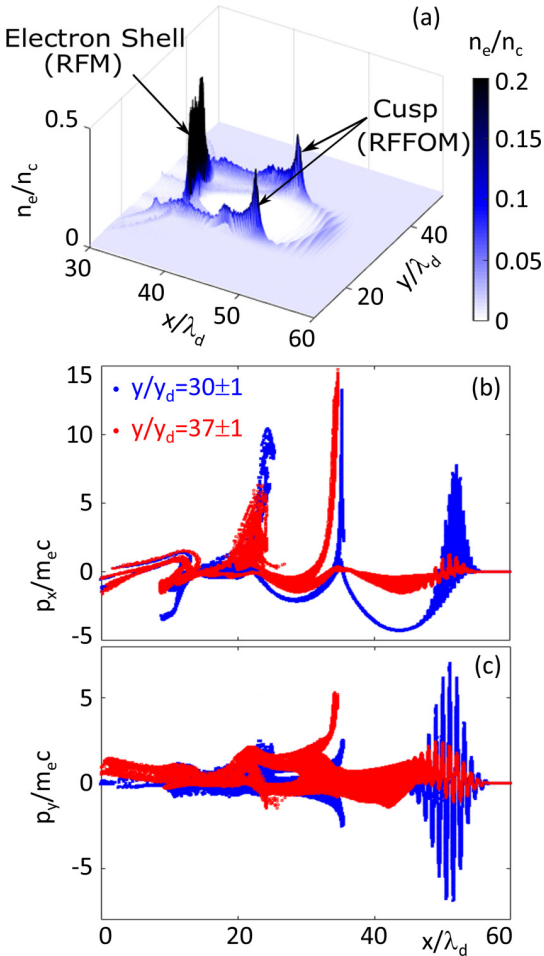


FIG. 5. (a) Electron density distribution in the  $(x, y)$  plane at  $t = 54T_d$ . (b) Longitudinal  $p_x$  and (c) transverse  $p_y$  electron momenta vs the  $x$  coordinate, for electrons in the strip near the axis  $29\lambda_d \leq y \leq 31\lambda_d$  (blue) and in the strip containing the cusp  $36\lambda_d \leq y \leq 38\lambda_d$  (red).

the cusped mirror with different inclination angle with respect to the driver axis.

Near the cusp, the electron density is comparable to that at the cavity rear, at the breaking point of the wake wave. Both the cusped mirror and the electron shell at the cavity rear provide efficient reflection due to strong localization of electrons. In addition, grazing incidence enhances the cusped mirror reflectivity, although at the expense of the greater off-axis reflection angle and correspondingly the lower frequency upshift factor, as follows from the model in Sec. III.

## VI. HIGH-RESOLUTION 2D SIMULATIONS

In order to see the spectral properties of the reflected radiation, we performed 2D PIC simulations in the moving window with higher resolution, for a grid mesh size of  $\Delta x/\lambda_d = 1/1024$  and  $\Delta y/\lambda_d = 1/256$ . The conical cusped mirror seen in the 3D simulation appears in 2D simulation as two cusped mirrors [Fig. 5(a)], analogously to the cross section in Fig. 4(a). We note that the cusp maintains a stable structure for more than 150 driver laser cycles. The cusped

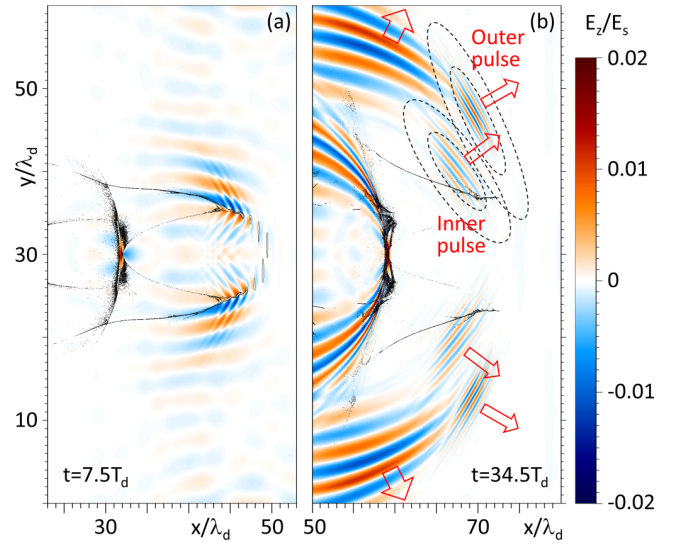


FIG. 6. Electric field  $E_z$  after the high-pass filter, for  $\omega \geq 2\omega_s$ , at (a)  $7.5T_d$  and (b)  $34.5T_d$ . The black thin curves correspond to electron densities of  $0.03n_c$ ,  $0.04n_c$ , and  $0.05n_c$ . Arrows show the propagation direction. Dashed ellipses show the reflected outer and inner pulses selected for spectrum analysis by the Gaussian spatial filters: The filter value is 0.999 for small ellipses and  $10^{-6}$  for larger ones.

mirror is a phase object; at each moment of time, it consists of different electrons, continuously flowing through it [29].

Figures 5(b) and 5(c) display the longitudinal  $p_x$  and transverse  $p_y$  momenta, respectively, for the electrons in different regions. The electrons located near the driver axis in a strip bounded as  $29\lambda_d \leq y \leq 31\lambda_d$  (shown in blue) demonstrate well-known patterns of the wake wave behind an intense short laser pulse. Characteristic modulations induced by the driver field indicate the location of the driver pulse. Longitudinal wave breaking is seen at  $x \approx 22\lambda_d$  and  $x \approx 35\lambda_d$  in Fig. 5(b); transverse wave breaking is seen at  $x \approx 33.5\lambda_d$  in Fig. 5(c).

The momentum distributions of electrons at the periphery, in the strip containing the cusp ( $36\lambda_d \leq y \leq 38\lambda_d$ ), are shown in red in Figs. 5(b) and 5(c). For electrons near the cusp, the longitudinal momentum  $p_x$  is negative [Fig. 5(b)], which means that these electrons move backward with respect to the  $x$  axis, in striking contrast to the motion of the cusp in the forward direction. The transverse momentum  $p_y$  of electrons near the cusp fills a relatively wide strip stretching from negative to positive values [Fig. 5(c)], which indicates a multistream flow.

Upon reflection from the cusped mirror, the source pulse transforms into several well-separated pulses with different wavelength and propagation direction, as seen in Fig. 6. Reflected pulses are almost bilaterally symmetric with respect to the  $x$  axis, which correlates with the approximate reflection symmetry of the cavity, bow waves, and cusps.

The pulses with the longest wavelength (the lowest frequency) are seemingly reflected from the outer side of the cusped mirror (farthest from the driver axis). They have a frequency multiplication factor of approximately 2.6 and propagate at an angle of approximately  $75^\circ$  with respect to the  $x$  axis, in accordance with the asymptotes in Eqs. (1) and (2).

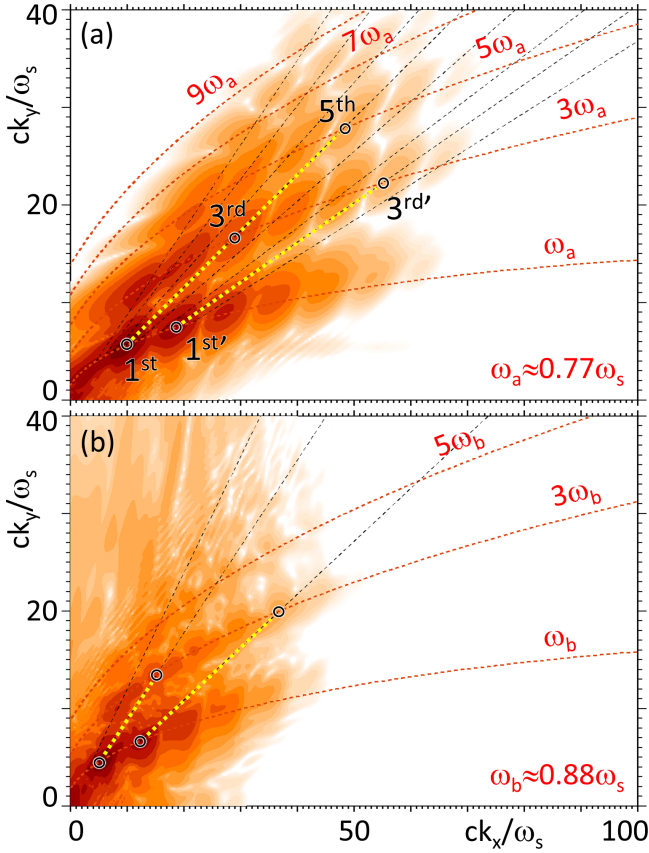


FIG. 7. Frequency spectrum of the (a) outer and (b) inner pulses selected by the Gaussian spatial filter shown in Fig. 6(b). Red dashed curves represent the frequency upshift dependence on the reflection angle  $\phi_r = \arctan(k_y/k_x)$  [Eq. (5)], where  $\omega_s$  is replaced by the odd harmonics of  $\omega_a$  and  $\omega_b$ . Radial black dotted lines are for (a)  $22^\circ \pm 1.8^\circ$ ,  $30^\circ \pm 3^\circ$ ,  $37^\circ$ , and  $41^\circ$  and (b)  $28.5^\circ$ ,  $41.5^\circ$ , and  $50^\circ$ . Black circles emphasize the peaks in the frequency spectrum corresponding to the harmonics and diffraction orders.

The pulses with the shorter wavelengths (higher frequencies) are reflected from both sides of the cusped mirror. The outer pulse propagates away from the  $x$  axis, while the inner pulse initially propagates toward the  $x$  axis. In the upper half plane in Fig. 6(b), the outer pulse originates from the top of the cusped mirror at  $y > 30\lambda_d$ , while the inner pulse originates from top of the cusped mirror at  $y < 30\lambda_d$ .

The strikingly different wavelength and propagation direction of the reflected well-separated pulses indicate that reflection occurs at a relativistic flying reflective diffraction grating. In addition to a specularly reflected wave, the grating diffracts the incident wave at different angles. Due to the Doppler effect, the frequency upshift factor is greater for smaller diffraction (reflection) angles, according to Eqs. (1) and (5).

The outer and inner pulses contain high-order harmonics due to oscillations of the reflecting facets of the cusped mirror imposed by the driver laser. Their spatial spectra are shown in Fig. 7. The spectra resemble an opened folding fan. The distribution of the electromagnetic energy density is discretized with respect to both the angle and the wave number

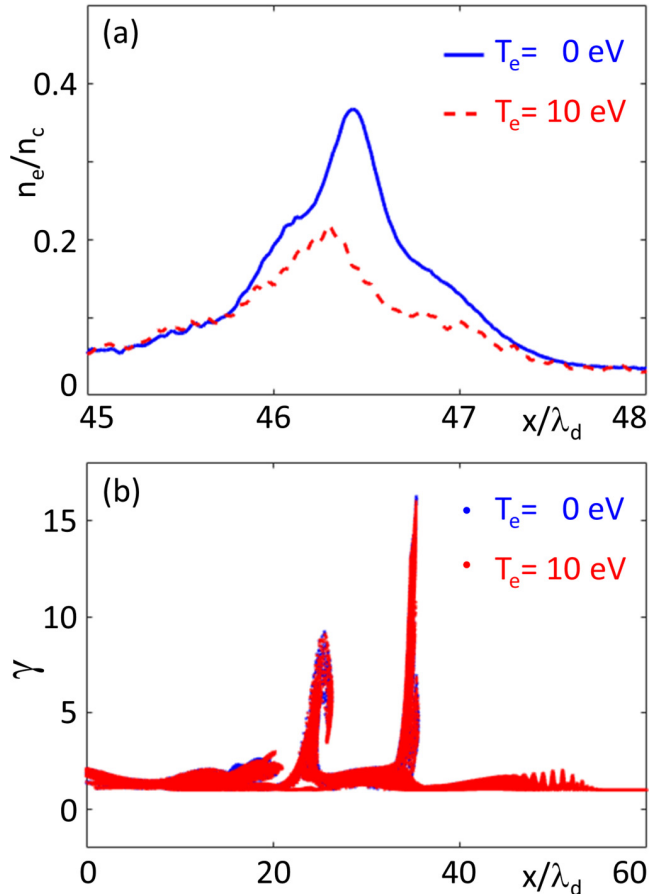


FIG. 8. (a) Cross section of the electron density near the cusp at  $y = 36.67\lambda_d$  and (b) the Lorentz factor  $\gamma$  of electrons near the cusp in the strip bounded as  $36 \leq y \leq 38\lambda_d$ , for two simulations with different initial electron temperature. The result for  $T_e = 0$  eV is marked in blue (hardly visible); the result for  $T_e = 10$  eV is marked in red.

(or frequency). The discretization with respect to the angle corresponds to the property of the cusped mirror to act as a reflective diffraction grating. The discretization with respect to the wave number (or frequency) reveals high-order harmonic generation due to the cusped mirror oscillations induced by the driver pulse. The well-separated hot spots in Fig. 7 represent diffraction orders along the angle and harmonic orders along the wave number (or frequency).

The cusped mirror moves with the velocity close to the group velocity of the driver pulse,  $\beta = \sqrt{1 - \omega_{pe}^2/\omega_d^2} \approx 0.995$ ; the corresponding Lorentz factor is  $\gamma = \omega_d/\omega_{pe} = 10$ . The source pulse has a relatively low frequency; therefore, its wavelength inside plasma is longer than in vacuum,  $\tilde{\lambda}_s \approx 1.67\lambda_s$ . According to Eq. (5), the frequency upshift factor for radiation reflected at  $30^\circ$  with respect to the driver pulse axis is  $\omega_r/\omega_s \approx 11.4$ . This is in good agreement with the position of the first harmonic (hot spot) emitted at the above-specified angle in Fig. 7(a). The hot spots are arranged along curves close to ellipses defined by Eq. (5). Each curve corresponds to an odd harmonic of somewhat downshifted frequency of the source pulse.

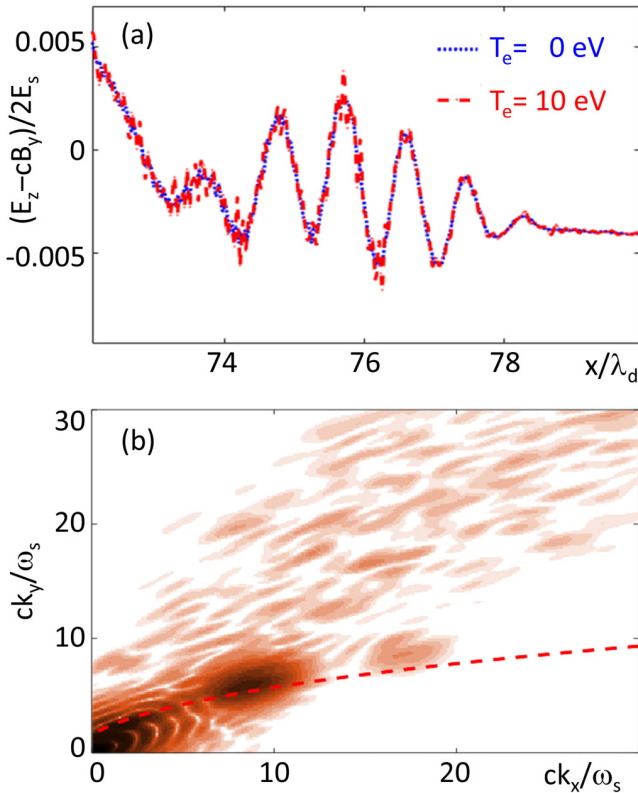


FIG. 9. (a) Combination of the electromagnetic field components  $E_z - cB_y$ , approximately representing reflected radiation, at  $y = 52\lambda_d$ . The blue dotted curve shows the initial electron temperature  $T_e = 0$  eV (blue) and the red dashed line  $T_e = 10$  eV. (b) Frequency spectrum of the outer pulse (color scale) and the ellipse representing the frequency upshift dependence (red dashed curve) as in Fig. 7(a), but for the initial electron temperature  $T_e = 10$  eV.

The energy of the outer pulse is estimated as  $\mathcal{E}_{OP} = 2.1 \times 10^{-7}$  J, or 0.53% of the source pulse. The corresponding number of photons is  $\mathcal{N}_{OP} = 6.4 \times 10^{11}$ . The reflection efficiency increases with the intensity of the driver pulse. For a driver pulse intensity of  $I_d^{PW} = 5.4 \times 10^{20}$  W/cm<sup>2</sup>, the outer pulse amplitude becomes  $1.21 \times 10^{10}$  V/m, 30.25% of the incident source pulse. The energy and number of photons increase to  $\mathcal{E}_{OP}^{PW} = 2.05 \times 10^{-6}$  J (1.02% of the source) and  $\mathcal{N}_{OP}^{PW} = 5.17 \times 10^{12}$ , respectively.

The reflectivity of the RFFOM seen in simulations requires further analytical investigation. Neglecting the forced oscillations of the mirror and correspondingly the generation of high-order harmonics, as in the model discussed in Sec. III, one can use the analytical results of Ref. [34] to calculate the reflectivity of various electron density singularities. Here the reflecting singularity consists of the cusp and two folds; the nearly flat fronts of the reflected radiation near the cusped mirror in Figs. 4(a) and 6 indicate that for such fronts the reflecting entity is a fold singularity.

## VII. THERMAL EFFECTS

In the description above, the initial electron temperature is assumed to be zero. Thermal effects on the RFM are analyzed

in Refs. [35–37]. An important factor for RFM wave breaking due to thermal effects can be mitigated by using tailored underdense plasma [38].

We note that the electron temperature in the location of an intense femtosecond laser pulse during its propagation in underdense plasma has not been measured in experiments; the estimates mentioned in the literature are based on the time-integrated observations with a typical timescale greater than 100 fs (e.g., Ref. [39]). In contrast, there are experimental measurements inconsistent with the assumption of a significant electron temperature at the location of a femtosecond laser pulse. They are represented by (i) a direct observation of a subtle structure of the wake wave by frequency-domain holography [40] and a femtosecond probe pulse [41], (ii) the measurements of the reflected spectrum and reflectivity of the RFM [9–11], and (iii) the detection of harmonics well resolved up to an order of a few hundredths from the laser self-focusing position [27,28,42] and the observation of a submicrometer pointlike sources of these harmonics [29].

In order to see how the electron temperature in the wake field modifies our scheme, we performed an additional 2D PIC simulation with an initial electron temperature of  $T_e = 10$  eV along the y-axis direction. As can be seen in Fig. 8(a), the maximum electron density corresponding to the cusp decreases by approximately 43%. The Lorentz factor of the electrons near the cusp for the initial electron temperature  $T_e = 10$  eV in Fig. 8(b) has almost the same pattern as in the case of zero initial temperature.

The outer pulse magnitude remains almost the same, as shown in Fig. 9(a), and at least the third harmonic of the upshifted base frequency can be seen. This means that the constructive interference condition for the formation of an optically coherent reflected radiation is still satisfied due to a strong localization of electrons in the cusped mirror. We note that an efficient reflection occurs also in regions where a singularity is present in the derivative of the electron density, as in the case of the wake wave breaking in thermal plasma [35,36].

## VIII. CONCLUSION

With the help of numerical simulations, we have found a physical realization of the relativistic mirror, the relativistic flying forcibly oscillating mirror. It combines the properties of the relativistic flying mirror [8] and relativistic oscillating mirror [17]. In addition, due to strong periodic modulations of the mirror surface, it acts as a reflective diffraction grating.

The RFFOM appears as a cusped mirror, the low-dimensional region of highest electron density at the joining of the electron cavity wall and the bow wave excited by the intense laser pulse (driver) propagating in plasma. It corresponds to an arrangement of universal and structurally stable density singularities, explained by catastrophe theory. The cusped mirror undergoes forced oscillations imposed by the driver pulse and moves with the group velocity of the driver. It efficiently reflects a counterpropagating relatively weak laser pulse (source). The reflected radiation spectrum exhibits well-pronounced diffractive orders and harmonic orders. These

characteristic features reveal that the cusped mirror is a relativistic flying and oscillating reflective diffraction grating. The base frequency of the reflected radiation and correspondingly all harmonic orders are strongly upshifted with respect to the base frequency of the incident source pulse, due to the double Doppler effect. In the wave number space, the harmonic orders are arranged along ellipsoids with one focus corresponding to the zero wave number.

The described scheme can be used for the generation of bright sources of high-frequency radiation. Its realization is easier than the RFM based on the reflection from the longitudinally breaking wake wave described in Refs. [8–11], where one should maintain a sufficiently slow approach to longitudinal wave breaking. While relativistic self-focusing may cause rapid longitudinal wave breaking destroying the RFM, it helps the discussed RFFOM realization.

Moreover, the described scheme provides an additional tool in laser plasma diagnostics, helping to analyze the dynamics of nonlinear physical processes in relativistic plasmas. The peculiar spectrum of the reflected radiation in the RFFOM scheme, using the head-on collision of the driver and source, substantially extends the capabilities of the scheme for probing relativistic plasma singularities by a transverse source pulse, suggested in Ref. [43]. By probing the cusped mirror by a weak counterpropagating short laser pulse, one can deduce or characterize the parameters of the laser-plasma interaction, including the geometrical properties of the first period of the wake wave (cavity and bow wave), driver pulse frequency and magnitude at the location of the cusped mirror, the velocity of the wake wave, the electron temperature or the electron

momentum distribution at the position of the cusped mirror, etc.

One of the immediate applications of such a diagnostic is control and tuning of burst intensification by singularity emitting radiation (BISER) [27–29,42], which occurs with the same parameters for the driver laser and plasma as required by the RFFOM, so that off-axis radiation from the RFFOM can be observed simultaneously with near- or on-axis BISER. In addition to the fundamental physics concerning intense laser-plasma interactions, plasma diagnostics with the described scheme may help to substantially improve the quality of the laser pulse, our main instrument, by revealing what laser parameters are the most critical. Such investigations, in the example of the laser pulse quality effects on the BISER realization, were conducted recently [44]. That work revealed some critical parameters of the laser pulse which must be improved to obtain good results and scalings predicted by theory.

## ACKNOWLEDGMENTS

We appreciate discussions with M. Matys. The work was supported by the project High Field Initiative (Grant No. CZ.02.1.01/0.0/0.0/15\_003/0000449) from the European Regional Development Fund, and the project “IT4Innovations National Supercomputing Center LM2015070” from the Ministry of Education, Youth and Sports in Czech Republic. We acknowledge support from JSPS KAKENHI Grants No. JP16K05639 and No. JP19H00669 and Strategic Grant by the QST President: Creative Research No. 20.

- 
- [1] F. Krausz and M. Ivanov, *Rev. Mod. Phys.* **81**, 163 (2009).
  - [2] G. A. Mourou, T. Tajima, and S. V. Bulanov, *Rev. Mod. Phys.* **78**, 309 (2006).
  - [3] A. Einstein, *Ann. Phys. (Leipzig)* **322**, 891 (1905).
  - [4] K. Landecker, *Phys. Rev.* **86**, 852 (1952).
  - [5] V. I. Semenova, *Sov. Radiophys. Quantum Electron.* **10**, 599 (1967).
  - [6] R. L. Savage, Jr., C. Joshi, and W. B. Mori, *Phys. Rev. Lett.* **68**, 946 (1992).
  - [7] A. Zhidkov, T. Esirkepov, T. Fujii, K. Nemoto, J. Koga, and S. V. Bulanov, *Phys. Rev. Lett.* **103**, 215003 (2009).
  - [8] S. V. Bulanov, T. Esirkepov, and T. Tajima, *Phys. Rev. Lett.* **91**, 085001 (2003).
  - [9] M. Kando, Y. Fukuda, A. S. Pirozhkov, J. Ma, I. Daito, L. M. Chen, T. Z. Esirkepov, K. Ogura, T. Homma, Y. Hayashi, H. Kotaki, A. Sagisaka, M. Mori, J. K. Koga, H. Daido, S. V. Bulanov, T. Kimura, Y. Kato, and T. Tajima, *Phys. Rev. Lett.* **99**, 135001 (2007).
  - [10] A. S. Pirozhkov, J. Ma, M. Kando, T. Z. Esirkepov, Y. Fukuda, L.-M. Chen, I. Daito, K. Ogura, T. Homma, Y. Hayashi *et al.*, *Phys. Plasmas* **14**, 123106 (2007).
  - [11] M. Kando, A. S. Pirozhkov, K. Kawase, T. Z. Esirkepov, Y. Fukuda, H. Kiriyama, H. Okada, I. Daito, T. Kameshima, Y. Hayashi *et al.*, *Phys. Rev. Lett.* **103**, 235003 (2009).
  - [12] S. V. Bulanov, T. Z. Esirkepov, M. Kando, A. S. Pirozhkov, and N. N. Rosanov, *Phys. Usp.* **56**, 429 (2013).
  - [13] M. Kando, T. Z. Esirkepov, J. K. Koga, A. S. Pirozhkov, and S. V. Bulanov, *Quantum Beam Sci.* **2**, 9 (2018).
  - [14] J. K. Koga, S. V. Bulanov, T. Z. Esirkepov, M. Kando, S. S. Bulanov, and A. S. Pirozhkov, *Plasma Phys. Contr. Fusion* **60**, 074007 (2018).
  - [15] V. V. Kulagin, V. A. Cherepenin, M. S. Hur, and H. Suk, *Phys. Plasmas* **14**, 113101 (2007).
  - [16] S. S. Bulanov, A. Maksimchuk, K. Krushelnick, K. I. Popov, V. Y. Bychenkov, and W. Rozmus, *Phys. Lett. A* **374**, 476 (2010).
  - [17] S. V. Bulanov, N. M. Naumova, and F. Pegoraro, *Phys. Plasmas* **1**, 745 (1994).
  - [18] N. M. Naumova, J. A. Nees, I. V. Sokolov, B. Hou, and G. A. Mourou, *Phys. Rev. Lett.* **92**, 063902 (2004).
  - [19] U. Teubner and P. Gibbon, *Rev. Mod. Phys.* **81**, 445 (2009).
  - [20] T. Z. Esirkepov, S. V. Bulanov, M. Kando, A. S. Pirozhkov, and A. G. Zhidkov, *Phys. Rev. Lett.* **103**, 025002 (2009).
  - [21] T. Tajima and J. M. Dawson, *Phys. Rev. Lett.* **43**, 267 (1979).
  - [22] A. Pukhov and J. Meyer-Ter-Vehn, *Appl. Phys. B* **74**, 355 (2002).
  - [23] E. Esarey, C. B. Schroeder, and W. P. Leemans, *Rev. Mod. Phys.* **81**, 1229 (2009).
  - [24] S. V. Bulanov, F. Pegoraro, A. M. Pukhov, and A. S. Sakharov, *Phys. Rev. Lett.* **78**, 4205 (1997).
  - [25] T. Z. Esirkepov, Y. Kato, and S. V. Bulanov, *Phys. Rev. Lett.* **101**, 265001 (2008).

- [26] T. Poston and I. Stewart, *Catastrophe Theory and Its Applications* (Dover, New York, 1996).
- [27] A. S. Pirozhkov, M. Kando, T. Z. Esirkepov, P. Gallegos, H. Ahmed, E. N. Ragozin, A. Y. Faenov, T. A. Pikuz, T. Kawachi, A. Sagisaka *et al.*, *Phys. Rev. Lett.* **108**, 135004 (2012).
- [28] A. S. Pirozhkov, M. Kando, T. Z. Esirkepov, P. Gallegos, H. Ahmed, E. N. Ragozin, A. Y. Faenov, T. A. Pikuz, T. Kawachi, A. Sagisaka *et al.*, *New J. Phys.* **16**, 093003 (2014).
- [29] A. S. Pirozhkov, T. Z. Esirkepov, T. A. Pikuz, A. Y. Faenov, K. Ogura, Y. Hayashi, H. Kotaki, E. N. Ragozin, D. Neely, H. Kiriyma *et al.*, *Sci. Rep.* **7**, 17968 (2017).
- [30] D. F. Gordon, B. Hafizi, D. Kaganovich, and A. Ting, *Phys. Rev. Lett.* **101**, 045004 (2008).
- [31] T. D. Arber, K. Bennett, C. S. Brady, A. L. Douglas, M. G. Ramsay, N. J. Sirccombe, P. Gillies, R. G. Evans, H. Schmitz, A. R. Bell *et al.*, *Plasma Phys. Contr. Fusion* **57**, 113001 (2015).
- [32] T. Esirkepov, *Comput. Phys. Commun.* **135**, 144 (2001).
- [33] P. Valenta, T. Z. Esirkepov, J. Koga, A. S. Pirozhkov, M. Kando, T. Kawachi, Y.-K. Liu, P. Fang, P. Chen, J. Mu *et al.*, *Phys. Plasmas* **27**, 032109 (2020).
- [34] A. V. Panchenko, T. Z. Esirkepov, A. S. Pirozhkov, M. Kando, F. F. Kamenets, and S. V. Bulanov, *Phys. Rev. E* **78**, 056402 (2008).
- [35] S. V. Bulanov, T. Z. Esirkepov, M. Kando, J. Koga, A. S. Pirozhkov, T. Nakamura, S. S. Bulanov, C. B. Schroeder, E. Esarey, F. Califano *et al.*, *Phys. Plasmas* **19**, 113102 (2012).
- [36] S. V. Bulanov, T. Z. Esirkepov, M. Kando, J. Koga, A. S. Pirozhkov, T. Nakamura, S. S. Bulanov, C. B. Schroeder, E. Esarey, F. Califano *et al.*, *Phys. Plasmas* **19**, 113103 (2012).
- [37] A. A. Solodov, V. M. Malkin, and N. J. Fisch, *Phys. Plasmas* **13**, 093102 (2006).
- [38] J. Mu, F. Y. Li, M. Zeng, M. Chen, Z. M. Sheng, and J. Zhang, *Appl. Phys. Lett.* **103**, 261114 (2013).
- [39] C. Zhang, C. K. Huang, K. A. Marsh, C. E. Clayton, W. B. Mori, and C. Joshi, *Sci. Adv.* **5**, eaax4545 (2019).
- [40] N. H. Matlis, S. Reed, S. S. Bulanov, V. Chvykov, G. Kalintchenko, T. Matsuoka, P. Rousseau, V. Yanovsky, A. Maksimchuk, S. Kalmykov *et al.*, *Nat. Phys.* **2**, 749 (2006).
- [41] A. Savert, S. P. D. Mangles, M. Schnell, E. Siminos, J. M. Cole, M. Leier, M. Reuter, M. B. Schwab, M. Möller, K. Poder, O. Jackel, G. G. Paulus, C. Spielmann, S. Skupin, Z. Najmudin, and M. C. Kaluza, *Phys. Rev. Lett.* **115**, 055002 (2015).
- [42] A. Sagisaka, K. Ogura, T. Z. Esirkepov, D. Neely, T. A. Pikuz *et al.*, *High Energy Density Phys.* **36**, 100751 (2020).
- [43] T. Z. Esirkepov, J. Mu, Y. Gu, T. M. Jeong, P. Valenta, O. Klimo, J. K. Koga, M. Kando, D. Neely, G. Korn, S. V. Bulanov, and A. S. Pirozhkov, *Phys. Plasmas* **27**, 052103 (2020).
- [44] A. S. Pirozhkov, T. Z. Esirkepov, T. A. Pikuz, A. Y. Faenov, A. Sagisaka *et al.*, *Quantum Beam Sci.* **2**, 7 (2018).